Delft University of Technology

Reconstruction of Directional Spectra of Infragravity Waves

Matsuba, Yoshinao; Roelvink, Dano; Reniers, Ad J.H.M.; Rijnsdorp, Dirk P.; Shimozono, Takenori

DOI
10.1029/2021JC018273

Publication date
2022

Document Version
Final published version

Published in
Journal of Geophysical Research: Oceans

Citation (APA)
Matsuba, Y., Roelvink, D., Reniers, A. J. H. M., Rijnsdorp, D. P., & Shimozono, T. (2022). Reconstruction of Directional Spectra of Infragravity Waves. *Journal of Geophysical Research: Oceans*, *127*(7), Article e2021JC018273. https://doi.org/10.1029/2021JC018273

Important note
To cite this publication, please use the final published version (if applicable).
Please check the document version above.

Copyright
Other than for strictly personal use, it is not permitted to download, forward or distribute the text or part of it, without the consent of the author(s) and/or copyright holder(s), unless the work is under an open content license such as Creative Commons.

Takedown policy
Please contact us and provide details if you believe this document breaches copyrights.
We will remove access to the work immediately and investigate your claim.

This work is downloaded from Delft University of Technology.
For technical reasons the number of authors shown on this cover page is limited to a maximum of 10.

Green Open Access added to TU Delft Institutional Repository

'You share, we take care!' - Taverne project

https://www.openaccess.nl/en/you-share-we-take-care

Otherwise as indicated in the copyright section: the publisher is the copyright holder of this work and the author uses the Dutch legislation to make this work public.

Check for updates

JGR Oceans

RESEARCH ARTICLE
10.1029/2021JC018273

Key Points:

- A new method to reconstruct directional spectra of free infragravity waves based on weakly nonlinear wave theory is proposed
- The method is verified to accurately reconstruct directional spectra of free infragravity waves from synthetic data
- Directional distributions of free infragravity waves vary diversely owing to wave reflection from nearby beaches and coastal structures

Supporting Information:

Supporting Information may be found in the online version of this article.

Correspondence to:

Y. Matsuba,
y.matsuba@un-ihe.org

Citation:

Matsuba, Y., Roelvink, D., Reniers, A. J. H. M., Rijnsdorp, D. P., & Shimozono, T. (2022). Reconstruction of directional spectra of infragravity waves. *Journal of Geophysical Research: Oceans*, *127*, e2021JC018273. https://doi.org/10.1029/2021JC018273

Received 10 DEC 2021
Accepted 25 JUN 2022

© 2022. American Geophysical Union. All Rights Reserved.

Reconstruction of Directional Spectra of Infragravity Waves

Yoshinao Matsuba[1], Dano Roelvink[1], Ad J. H. M. Reniers[2], Dirk P. Rijnsdorp[2], and Takenori Shimozono[3]

[1]IHE Delft Institute for Water Education, Delft, The Netherlands, [2]Delft University of Technology, Delft, The Netherlands, [3]The University of Tokyo, Tokyo, Japan

Abstract Understanding directional spectra of infragravity (IG) waves composed of free and bound components is required due to their impacts on various coastal processes (e.g., coastal inundation and morphological change). However, conventional reconstruction methods of directional spectra relying on linear wave theory are not applicable to IG waves in intermediate water depths (20–30 m) due to the presence of bound waves. Herein, a novel method is proposed to reconstruct directional spectra of IG waves in intermediate depth based on weakly nonlinear wave theory. This method corrects cross-spectra among observed wave signals by taking account of the nonlinearity of bound waves in order to reconstruct directional spectra of free IG waves. Numerical experiments using synthetic data representing various directional distributions show that the proposed method reconstructs free IG wave directional spectra more accurately than the conventional method. The method is subsequently applied to observations of severe sea-states at two field sites. At these sites, free IG waves are not isotropic and have clear peak directions. Numerical modeling of the wave fields shows that these peak directions correspond to the reflection of IG waves from the shore and/or coastal structures. Additionally, the validity of the underlying weakly nonlinear wave theory of the present method is assessed by a newly proposed method employing bispectral analysis. The bound wave response generally agrees with the theory at the field sites but deviates slightly for energetic sea states. The applicability of the present method on a sloping bottom is further discussed by an analytical solution.

Plain Language Summary Infragravity (IG) waves, long waves whose wave period is much longer than sea and swells, are known to play important roles in coastal inundation and beach topographic change during high wave conditions. However, the magnitude of IG waves propagating to beaches is not well understood. This is because conventional methods to estimate directional distributions (wave energy propagating to each direction) of sea and swells are not applicable to IG waves that are composed of "free" and "bound" components. In this study, a novel method to estimate directional distributions of IG waves is proposed. The method estimates directional distributions of free IG waves by considering bound IG waves in observed wave data based on their theoretical solution. This method is tested in numerical experiments using synthetic wave data, and the results demonstrate its high applicability and superiority over the conventional method. Applying this method to field measurement data reveals that free IG waves are directionally focused owing to the reflection from the shore and coastal structures. These findings violate the assumption of uniform directional distributions of free IG waves implemented in recent numerical models. The new method will help future studies to elucidate the magnitude of IG waves propagating to beaches.

1. Introduction

While a large portion of the offshore wave energy is composed of sea and swell (>0.04 Hz, SS waves hereafter), long wave components (0.005–0.04 Hz) often referred to as infragravity (IG) waves are known to develop in shallow water (Bertin et al., 2018). IG waves are excited as "bound waves" in the shoaling zone, which propagate being bound to incident wave groups (Biésel, 1952; Longuet-Higgins & Stewart, 1962). Depending on the near-shore characteristics and wave conditions (e.g., steep vs. mild sloping beaches, stormy vs. calm), they may lose a portion of their energy in the surf-zone (Bertin et al., 2020; de Bakker et al., 2014; Henderson et al., 2006; Inch et al., 2017; van Dongeren et al., 2007). After (partial) reflection at the shoreline, free IG waves (no longer bound to their forcing) radiate seaward (Herbers et al., 1995). Free IG waves are also known to be excited by dynamic setup and setdown owing to varying breakpoint of incident wave groups (Symonds et al., 1982). IG waves are known to enhance coastal damage during extreme conditions (Roeber & Bricker, 2015), cause seiches in harbors (Okihiro et al., 1993), and change beach topography (McCall et al., 2010; Roelvink et al., 2009). Therefore, it

is important to understand the evolution of IG waves. In particular, free and bound IG waves (hereafter FIG and BIG waves) behave differently because FIG waves are the first-order waves while BIG waves are the second-order waves.

The characteristics of FIG waves can be described with linear wave theory. The amplification of FIG waves follows Green's law, but their magnitude is highly affected by wave refraction due to their long wavelengths. Most of the reflected FIG waves are expected to be trapped due to wave refraction and residuals leak to offshore as leaky waves (Herbers et al., 1995; Okihiro et al., 1992). The trapped waves can generate an alongshore standing wave structure, which intensifies the local magnitude of IG waves (Thomson et al., 2007; Winter et al., 2017). The leaky waves are known to be able to cross ocean basins and reach distant coastlines (Ardhuin et al., 2014; Rawat et al., 2014). In contrast, BIG waves cannot be described by linear theory due to their nonlinearity. An equilibrium solution of BIG waves in uniform depth was derived based on weakly nonlinear wave theory (Hasselmann, 1962). Recent studies have found that their characteristics deviate from this homogenous solution on a sloping bottom (e.g., Battjes et al., 2004; Contardo et al., 2021; Janssen et al., 2003; Nielsen & Baldock, 2010). These locally forced IG waves are bound to their forcing, and they are amplified as water depth decreases with an amplification factor that exceeds Green's law. Therefore, locally amplified BIG waves are generally expected to be the dominant contributor to nearshore IG waves.

Recently developed numerical models such as SWASH (Zijlema et al., 2011) or XBeach (Roelvink et al., 2009) are inherently able to predict propagations of locally generated IG waves accurately (e.g., Bertin et al., 2020; Rijnsdorp et al., 2015). In general, predicted or observed directional spectra of SS waves are given at the offshore boundary in the models. BIG waves are implemented at the model boundary (Fiedler et al., 2019; Rijnsdorp et al., 2014, 2015) based on weakly nonlinear wave theory of Hasselmann (1962). In contrast, shoreward propagating FIG waves from the outside of the model domain are often neglected because of the huge uncertainty of their magnitude and directions. However, recent studies have found that incident FIG waves originating from remote beaches were not negligible during intensive storms (Matsuba et al., 2021a; Rijnsdorp et al., 2021). This suggests that including FIG waves at the model boundary, which can be generated from their directional spectra, may further improve local modeling of nearshore IG waves and their impact on coastal processes.

Conventional reconstruction methods of directional spectra assume that every wave component follows the first-order (linear) wave theory and neglect the influence of (nonlinear) higher-order waves (e.g., Isobe & Kondo, 1985). Nevertheless, recent advancement of the reconstruction methods of directional spectra has enabled us to obtain sufficiently accurate estimates of SS directional spectra in particular around the peak frequency (Barstow et al., 2005; Donelan et al., 2015; Hashimoto et al., 1995; Hashimoto & Kobune, 1988; Plant & Donelan, 2020), because SS wave components around the peak frequency follow the first-order wave theory outside the surf zone (e.g., Herbers et al., 2002; Martins et al., 2021). However, these conventional methods are not applicable to nearshore IG waves in particular during stormy conditions, because BIG waves are comparable or larger than FIG waves. Therefore, previous studies discussed directional spectra of IG waves only in shallow water around 10 m depth ($kh \ll 1$), where the behavior of BIG waves gets close to that of FIG waves (Herbers et al., 1995; Mahmoudof & Siadatmousavi, 2020; Nose et al., 2017). As a result, we lack the ability to estimate IG wave directional spectra accurately at intermediate water depth (~25 m, $kh < 1$) where both BIG and FIG waves are present.

To reveal magnitude and directions of IG waves consisting of BIG and FIG waves, we propose a new method to reconstruct IG directional spectra at intermediate water depths. The method enables us to obtain FIG wave directional spectra by considering the differences between BIG and FIG waves based on the weakly nonlinear wave theory by Hasselmann (1962). The validity of the new method and its superiority over conventional methods relying on linear wave theory were demonstrated by numerical experiments using synthetic data. Subsequently the method was applied to in-situ data during energetic conditions, which highlighted the diverse directional distributions of FIG waves. In the next section, the theoretical background of the new reconstruction method of directional spectra is introduced. Section 3 describes the in-situ data and the numerical experiments using synthetic data. Results of the numerical experiments and field application are shown in Section 4. The observed diverse directional distributions of FIG waves and validity of the weakly nonlinear wave theory are discussed in Section 5. The main findings of this study are summarized in Section 6.

2. Derivation of a New Reconstruction Method

2.1. Theory

To discuss a new approach to reconstruct directional spectra of IG waves, theoretical background is introduced basically following Hasselmann (1962) and Hasselmann et al. (1963). Hasselmann (1962) applied perturbation analysis to describe multi-directional irregular waves in uniform water depth and derived a solution at each order of the wave slope (μ). Hereafter Hasselmann (1962)'s theory is referred to as H62. Here, we consider the wave-related variable ξ_n, which can be water level change η, horizontal and vertical water velocities u and w, bottom pressure p, and others. In the perturbation expansion, ξ_n can be given by $\xi_n = \sum_j \xi_n^{(j)}$, with the superscript with parenthesis (j) indicating j-th order waves ($\sim O\left(\mu^j\right)$). Using the Stieltjes integral to describe multi-directional irregular wave fields (Hasselmann, 1962; Herbers et al., 1994), $\xi_n^{(j)}$ can be given by

$$\xi_n^{(j)} = \int_{f=0}^{\infty} d\xi_{n,f}^{(j)}. \tag{1}$$

Here, the subscript f means f-Hz component.

For the first-order waves, the f-Hz component of ξ_n can be defined as

$$d\xi_{n,f}^{(1)} = \int_{\theta} H_{n,f}^{(1)}(\theta) d A_f^{(1)}(\theta) \exp[i(\boldsymbol{k} \cdot \boldsymbol{x} - \omega t)] + \mathrm{CC}. \tag{2}$$

$dA_f^{(1)}(\theta)$ indicates the amplitude of a wave with frequency f and wave direction θ, $\boldsymbol{k}$ is the wavenumber vector $(k\cos\theta, k\sin\theta)$, ω is the angular frequency, $\boldsymbol{x}$ and t are space and time, respectively, and CC indicates the complex conjugate. $H_{n,f}^{(1)}(\theta)$ represents a transfer function that relates η to ξ_n for the (f, θ) component. Following these definitions, the one-sided cross-spectrum $\Phi_{mn}(f)$ between ξ_m and ξ_n can be defined as,

$$\Phi_{mn}(f)df = 2\left\langle \int_{\theta} H_{m,f}^{(1)*} dA_f^{(1)*}(\theta) \exp(-i\boldsymbol{k} \cdot \boldsymbol{x_m}) \int_{\theta'} H_{n,f}^{(1)} dA_f^{(1)}(\theta') \exp\left(i\boldsymbol{k}' \cdot \boldsymbol{x_n}\right) \right\rangle. \tag{3}$$

Here, $\langle\rangle$ indicates the ensemble average, the asterisk superscript indicates the complex conjugate, and $\boldsymbol{x_n}$ is the coordinate where ξ_n is observed.

If the wave field is Gaussian, $\langle dA_f^{(1)*}(\theta) dA_f^{(1)}(\theta')\rangle = 0$ when $\theta \neq \theta'$ and it becomes $\frac{1}{2}S^{(1)}(f,\theta) df d\theta$ when $\theta = \theta'$, where $S^{(1)}(f,\theta)$ is the (f,θ) component of the directional spectrum, and df and $d\theta$ are infinitely small bin widths of frequency and direction. By using this relationship, $\Phi_{mn}(f)$ can be simplified as

$$\Phi_{mn}(f) = \int H_{m,f}^{(1)*} H_{n,f}^{(1)} \exp[i\boldsymbol{k} \cdot (\boldsymbol{x_n} - \boldsymbol{x_m})] S^{(1)}(f,\theta) d\theta. \tag{4}$$

Based on this relationship, which provides the theoretical background of conventional methods, the directional spectrum $S^{(1)}(f,\theta)$ can be computed from cross-spectra among all pairs of observed wave-related variables. To compute directional spectra accurately from measured wave data, several methods that solve Equation 4 have been proposed (see Benoit et al. (1997) for a review).

For IG waves, however, this relationship does not hold owing to the presence of BIG waves which can be explained by the second-order wave theory. According to H62, a pair of two components of first-order waves (f_j, θ_j) excites a wave at the subharmonic frequency $f = |f_2 - f_1|$. Note that superharmonic components will be neglected in this study because we focus on IG frequencies. In uniform water depth, the amplitude of a BIG wave component is given by

$$dA_f^{(2)}(f_1, \theta_1, \theta_2) = 2dA_{f_1}^{(1)*}(\theta_1) dA_{f_2}^{(1)}(\theta_2) \Omega. \tag{5}$$

Here, Ω is a nonlinear coupling coefficient given by the following equations,

$$\Omega = -\frac{gk_1k_2\cos\Delta\theta}{2\omega_1\omega_2} - \frac{\omega_1\omega_2}{2g} + \frac{\left(\omega_1^2 + \omega_2^2\right)}{2g} + \Gamma, \tag{6a}$$

$$\Gamma = -\frac{g\omega}{\left[g\Delta k \tanh(\Delta kh) - \omega^2\right]\omega_1\omega_2}\left\{\omega\left[\left(\frac{\omega_1\omega_2}{g}\right)^2 + k_1k_2\cos\Delta\theta\right] - \frac{1}{2}\left[\frac{\omega_1 k_2^2}{\cosh^2(k_2h)} - \frac{\omega_2 k_1^2}{\cosh^2(k_1h)}\right]\right\}. \tag{6b}$$

Here, g is the gravitational acceleration, h is the still water depth, and $\Delta\theta = \theta_2 - \theta_1$. k_j and ω_j indicate the wavenumber and angular frequency of (f_j, θ_j) component satisfying $\omega_j^2 = gk_j \tanh k_j h$. The difference wavenumber vector $\Delta\boldsymbol{k}$ is $\boldsymbol{k}_2 - \boldsymbol{k}_1$, with modulus $\Delta k = \sqrt{k_1^2 + k_2^2 - 2k_1k_2\cos\Delta\theta}$. The f-Hz components of $\xi_n^{(2)}$ are given as the integration of every pair satisfying $f = f_2 - f_1$ as follow:

$$d\xi_{n,f}^{(2)} = \int_{f_1=0}^{\infty}\int_{\theta_1}\int_{\theta_2} H_{n,f}^{(2)}(f_1,\theta_1,\theta_2)dA_f^{(2)}\exp[i(\Delta\boldsymbol{k}\cdot\boldsymbol{x} - \omega t)] + \mathrm{CC}. \tag{7}$$

Therefore, when second-order waves are not negligible and ξ_n is represented as $\xi_n^{(1)} + \xi_n^{(2)}$, the cross-spectrum between ξ_m and ξ_n is given by

$$\Phi_{mn}(f)df = 2\left\langle\left[\int_\theta H_{m,f}^{(1)^*}dA_f^{(1)^*}(\theta)\exp(-i\boldsymbol{k}\cdot\boldsymbol{x_m}) + \int_{f_1=0}^{\infty}\int_{\theta_1}\int_{\theta_2} H_{m,f}^{(2)^*}(f_1,\theta_1,\theta_2)\,dA_f^{(2)^*}\exp(-i\Delta\boldsymbol{k}\cdot\boldsymbol{x_m})\right]\right.$$
$$\left.\cdot\left[\int_{\theta'} H_{n,f}^{(1)}dA_f^{(1)}(\theta')\exp(i\boldsymbol{k}'\cdot\boldsymbol{x_n}) + \int_{f_1'=0}^{\infty}\int_{\theta_1'}\int_{\theta_2'} H_{n,f}^{(2)}(f_1',\theta_1',\theta_2')\,dA_f^{(2)}\exp(i\Delta\boldsymbol{k}'\cdot\boldsymbol{x_n})\right]\right\rangle. \tag{8}$$

For a Gaussian wave field, $\langle dA_f^{(1)*}dA_f^{(2)}\rangle$ is expected to vanish for every pair of wave components, and $\langle dA_f^{(2)*}dA_f^{(2)}\rangle$ also becomes zero unless $(f_1,\theta_1,\theta_2) = (f_1',\theta_1',\theta_2')$. When $(f_1,\theta_1,\theta_2) = (f_1',\theta_1',\theta_2')$, $\langle dA_f^{(2)*}dA_f^{(2)}\rangle$ becomes $S^{(1)}(f_1,\theta_1)\,S^{(1)}(f_2,\theta_2)\,\Omega^2 df^2 d\theta^2$. Therefore, considering the second-order waves results in the following equation:

$$\Phi_{mn}(f) = \int H_m^{(1)^*}H_n^{(1)}\exp[i\boldsymbol{k}\cdot(\boldsymbol{x_n} - \boldsymbol{x_m})]\,S^{(1)}(f,\theta)d\theta + 2\int\int\int H_{m,f}^{(2)^*}H_{n,f}^{(2)}\exp[i\Delta\boldsymbol{k}\cdot(\boldsymbol{x_n} - \boldsymbol{x_m})]\,S^{(1)}(f_1,\theta_1)\,S^{(1)}(f_2,\theta_2)\,\Omega^2 df_1 d\theta_1 d\theta_2. \tag{9}$$

Here, for IG frequency components, the first term is related to FIG waves (here defined as $\Phi_{mn}^F(f)$) and the second term ($\Phi_{mn}^B(f)$) arises due to the presence of BIG waves.

If $H_{n,f}^{(2)} \cong H_{n,f}^{(1)}$ and $\Delta k \cong k$, Equation 9 can be simplified as $\Phi_{mn}(f) = \int H_m^{(1)^*}H_n^{(1)}\exp[i\boldsymbol{k}\cdot(\boldsymbol{x_n} - \boldsymbol{x_m})]\left[S^{(1)}(f,\theta) + S^{(2)}(f,\theta)\right]d\theta$ in the similar form of Equation 4 and thus $S^{(1)}(f,\theta) + S^{(2)}(f,\theta)$ can be obtained by conventional methods solving Equation 4. However, in general, $H_{n,f}^{(2)}$ and Δk are functions of (f_1,θ_1,θ_2) and deviate from $H_{n,f}^{(1)}$ and k. The velocity potential $d\phi^{(2)}(f_1,\theta_1,\theta_2)$ at the height of $h+z$ from the seabed is given as

$$d\phi^{(2)}(f_1,\theta_1,\theta_2) = \frac{g\Gamma\cosh\Delta k(h+z)}{i\Omega\omega\cosh\Delta kh}dA_f^{(2)}(f_1,\theta_1,\theta_2)\exp[i(\Delta\boldsymbol{k}\cdot\boldsymbol{x} - \omega t)] + \mathrm{CC}. \tag{10}$$

$H_{n,f}^{(2)}$ can be derived from $d\phi_f^{(2)}$ (see Supporting Information S2). Figure 1 shows $H_{n,f}^{(2)}/H_{n,f}^{(1)}$ of u, w, and p, and $\Delta k/k$ in colinear coupling cases ($\theta_1 = \theta_2$). The left panels correspond to the case where $h = 25$ m for u and w taken at 15 m from the bottom and p at the bottom. These parameters are representative for the values of in-situ measurement devices used in this study. As seen here, $H_p^{(2)}/H_p^{(1)}$ is close to unity when both f and f_1 are low, but it deviates for larger f. Significant deviations can be observed for u and w. $H_w^{(2)}/H_w^{(1)}$ is more than two for $f_1 = 0.10$ Hz. Moreover, $\Delta k/k$ deviates from unity. Therefore, the conventional methods that rely on first-order wave theory are not applicable to IG waves in intermediate water depths (~25 m) when second-order BIG waves are present. The right panels in Figure 1 show the case where $f_1 = 0.10$ Hz and h varies. The height for u and w

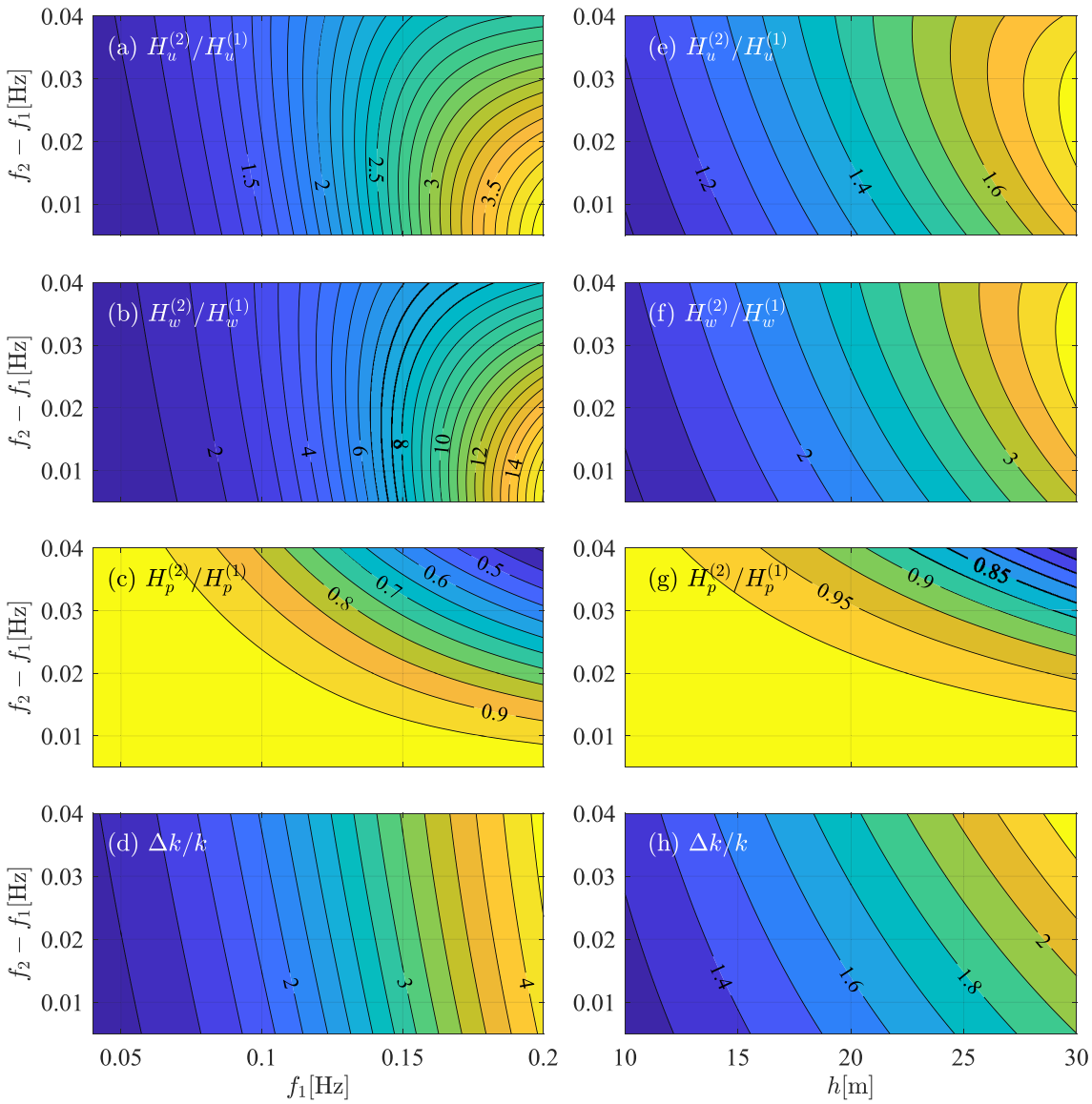

Figure 1. $H_{n,f}^{(2)}/H_{n,f}^{(1)}$ for horizontal velocity (a, e), vertical velocity (b, f), and bottom pressure (c, g) and $\Delta k/k$ (d, h). Left panels correspond to when h is fixed (25 m), and right to when f_1 is fixed (0.10 Hz).

is set to be $h/2$. The ratio gets close to unity following the decrease in h except $H_w^{(2)}/H_w^{(1)}$. However, $H_u^{(2)}/H_u^{(1)}$ and $\Delta k/k$ are still larger than 1.2 at 15 m depth. This indicates that, when BIG waves are not negligible, the conventional reconstruction method of directional spectra relying on linear wave theory is applicable only in shallow water (<∼10 m).

2.2. Proposed Method

To reconstruct directional spectra of IG waves, it is necessary to consider the presence of BIG waves which have different transfer functions and wavenumber than (linear) FIG waves. In general, the main driver of BIG waves in the shoaling zone is incident SS waves, especially around the peak frequency f_p (e.g., de Bakker et al., 2015). For example, interactions among components within $0.5 < f/f_p < 1.5$ account for more than 90% of BIG wave energy during representative wave conditions at any depths ranging 15–30 m (Supporting Information S1). Relatively high SS-frequency components may be composed of first-order waves and second-order waves (resulting from sum-interactions), but most of incident SS components around the peak frequency can be assumed to be first-order waves (e.g., Martins et al., 2021). Therefore, directional spectra of SS waves are expected to be

successfully reconstructed by the conventional methods. As long as an accurate directional spectrum of SS waves around the peak frequency is available and nonlinear couplings between FIG waves are negligible, the second term in Equation 9, Φ^B_{mn}, can be estimated theoretically.

Based on the abovementioned background, IG wave directional spectra can be reconstructed with the following steps:

1. Compute Φ_{mn} for all pairs of ξ_m and ξ_n.
2. Estimate a directional spectrum of SS waves $S_{\mathrm{SS}}(f,\theta)$ by solving Equation 4 using a conventional method.
3. Compute Φ^B_{mn} based on $S_{\mathrm{SS}}(f,\theta)$ from Equation 9.
4. Obtain Φ^F_{mn} as $\Phi^F_{mn} = \Phi_{mn} - \Phi^B_{mn}$.
5. Estimate a directional spectrum of FIG waves $S^F_{\mathrm{IG}}(f,\theta)$ by replacing Φ_{mn} with Φ^F_{mn} in Equation 4 and solving it.
6. Obtain a directional spectrum of BIG waves $S^B_{\mathrm{IG}}(f,\theta)$ by summing up all possible couplings between SS components following H62.

Any conventional method to solve Equation 4 can be applied in Step 2 and 5. Bayesian Directional Method (BDM) is employed in this study (e.g., Hashimoto & Kobune, 1988; Fujiki et al., 2017), which solves discretized Equation 4 considering smoothness of the directional distribution.

Theoretically, the present method requires a data set of three or more wave signals, and the requirement is not different from the one for conventional methods. At least one of the signals needs to be η or p (η is preferred to obtain accurate wave energy), and each pair of the different signals is required to satisfy $H^{(1)*}_{m,f}(\theta)H^{(1)}_{n,f}(\theta) \neq$ const. or $\boldsymbol{x_n} \neq \boldsymbol{x_m}$ (e.g., multiple η or p measured by an array of wave gauges, a set of η or p and u in different directions measured by a pair of wave gauge and current meter).

In addition to the general assumptions in the conventional methods (uniform water depth, Gaussian wave field, and so on), the proposed method relies on the following additional assumptions:

1. IG waves are composed of first-order FIG waves and second-order BIG waves.
2. BIG waves are dominantly excited by SS waves following H62.
3. Edge waves can be neglected.

The last assumption is required because edge waves have a different dispersion relation than Airy waves (Ursell, 1952). Due to their exponentially decaying cross-shore structure, edge waves can be generally neglected when the site is located at intermediate depths that is located sufficiently far from the shore (i.e., several IG wavelengths).

Additionally, we stress again that equilibrium solution of H62 is derived for uniform water depth and is thus formally not valid on a sloping bottom. Indeed, BIG wave heights are known to be overestimated by the equilibrium solution. Battjes et al. (2004) reported that the amplification factor of lower frequency BIG waves gets close to Green's law in shallow water. Another potential source of inaccuracy is related to the phase difference between IG waves and wave groups. According to H62, Ω is a negative real number when $\Delta\theta$ is small, that is, BIG waves are 180° out of phase with the wave groups. However, previous studies found that the phase difference deviates from 180° and IG waves lag behind the wave groups following a decrease in water depth (e.g., Contardo et al., 2021; Guérin et al., 2019; Janssen et al., 2003; Nielsen & Baldock, 2010 and many more). For these reasons, Φ^B_{mn} estimated by H62 may increase the estimation errors of S^F_{IG}. We will discuss the validity of H62 for the field sites considered in this study in Section 5.2.

3. Methods

3.1. In-Situ Observation by Directional Wave Meters

In this study, we use measurements from NOWPHAS (Nationwide Ocean Wave information network for Ports and Harbors) observatories in Japan. In the NOWPHAS system, more than 70 observatories are located near major ports and harbors around Japan at depth of around 20–50 m, and continuous wave observations are carried out using submerged Doppler-type directional wave meters (DWM hereafter, USW series by SONIC CORPORATION). A DWM uses ultrasonic beams to measure water surface elevation η. Moreover, it radiates ultrasonic beams to three different directions (β_M with $M = 1, 2, 3$) to measure water velocity profiles along the beams at

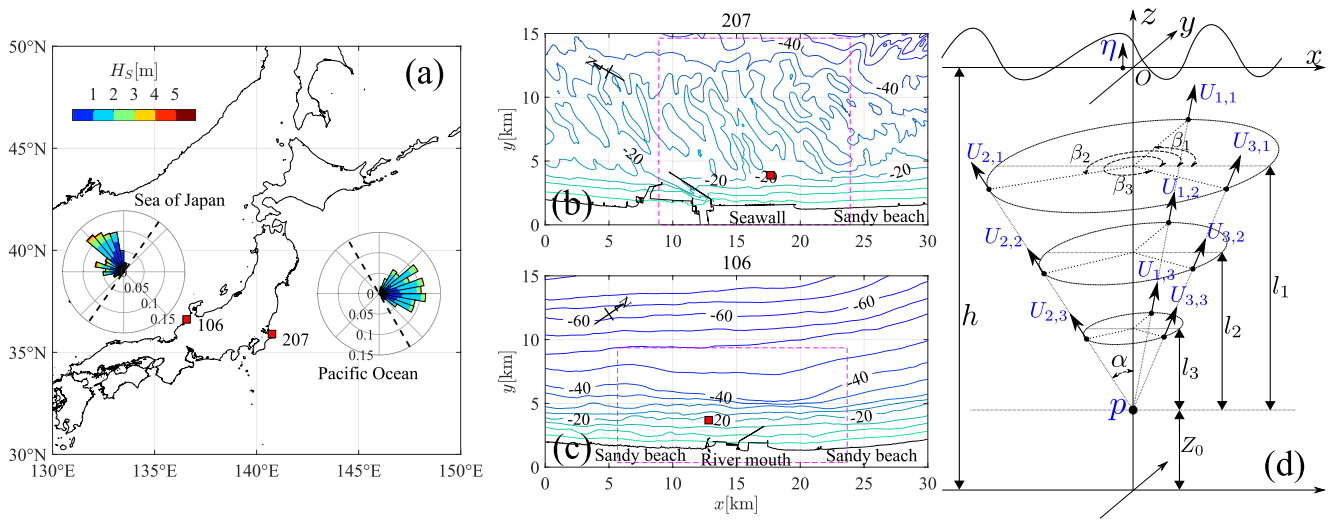

Figure 2. Overview of the field observation by NOWPHAS. (a) Locations of observatories and the wave climates. The dashed black lines indicate alongshore direction. (b, c) Bathymetry at 207 and 106. The dashed pink rectangles are computational domains for XBeach. (d) Observation by DWMs. Blue indicates measured wave properties.

three vertical layers (their heights from the device are defined as l_N with $N = 1, 2, 3$). The water velocity profiles are defined as $U_{M,N}$. Additionally, the device measures the water pressure p. Detailed measurement settings are shown in Figure 2d. In this figure, Z_0 is a height of a DWM from the seabed, α is the inclination of the beams for velocity measurements from the vertical axis ($\alpha = 30°$). β_M is positive in anticlockwise from the east ($\beta_M = 90°, 210°, 330°$). In total, 11 wave variables are continuously measured at a sampling rate of 2 Hz.

Two NOWPHAS observatories (207 and 106) were selected in this study because they face the open ocean and are in intermediate water depths ($h = 24.6$ and 21.1 m, respectively) that is sufficiently deep to prevent depth-induced wave breaking of energetic waves. The maximum ratio of individual wave height to still water depth ($H_{\max}/h$) during the observation (0.60) was less than the value of breaking onset (>0.7 in most cases in this study) by Battjes and Stive (1985). The measurement setting (Z_0, l_1, l_2, l_3) is (0.9, 13.7, 8.7, and 3.7 m) at 207 and (1.2, 12.4, 9.9, and 4.9 m) at 106, respectively. Their locations are shown in Figure 2a. 207 faces the Pacific Ocean and 106 faces the Sea of Japan. Both observatories are located near coastal structures. A 4-km long breakwater is located toward the north of 207 which protects the entrance of a large harbor, and the landward side of this observatory is also protected by a straight seawall (Figure 2b). In the south, a straight sandy coast extends. Similarly, a 2.5-km long breakwater is located at the east of 106, and the south coast is composed of straight sandy beaches (Figure 2c). Additionally, a small river mouth is located at the landward side of this observatory. In Figure 2a, the 5-year wave climates at both observatories are shown. Mean significant wave heights during the period are 1.3 and 1.1 m, but energetic waves (>5 m) are observed sometimes owing to passages of low-pressure systems and typhoons. The in-situ data during stormy conditions were utilized to test the present reconstruction method.

3.2. Numerical Experiments

In order to test the performance of the new method which can be deteriorated by several factors (e.g., errors from cross-spectral estimation and measurement noise) and demonstrate the improved accuracy of the present method over the conventional method, numerical experiments were conducted using synthetic data. Using idealized synthetic data is useful to compare performance of different reconstruction methods (e.g., Fujiki et al., 2017; Lin et al., 2022). We created synthetic data with settings that are representative for the measurement setting of the NOWPHAS observation ($h = 25$ m, and (Z_0, l_1, l_2, l_3) = (1, 15, 10, and 5 m)). Each variable is assumed to be a summation of the first-order SS components, the first-order IG components (FIG), and the second-order IG components (BIG) as given by

$$\xi_n = \xi^{(1)}_{n,\mathrm{SS}} + \xi^{(1)}_{n,\mathrm{IG}} + \xi^{(2)}_{n,\mathrm{IG}} + \epsilon. \tag{11}$$

Here, ϵ indicates white noise representing the observation error. Its magnitude was determined as 2% of the incident wave height referring to an average change rate of hourly observed significant wave heights at the

Table 1
Tested Parameters in the Numerical Experiments

	H_S (m)	f_p (Hz)	$\theta_{p1,\mathrm{IG}}$ (deg.)	$\theta_{p2,\mathrm{IG}} - \theta_{p1,\mathrm{IG}}$ (deg.)	m_{IG}
Unimodal	2, 4, 6	0.08	0, 45, 90, 135, 180	–	4, 10
Bimodal	5	0.08	90, 135, 180	135, 180, 225	4, 10
Isotropic	2, 4, 6	0.08, 0.10, 0.14	–	–	–

observatories. $\xi^{(1)}_{n,\mathrm{SS}}$ and $\xi^{(1)}_{n,\mathrm{IG}}$ were computed numerically based on linear wave theory following Equation 2. $|dA^{(1)}_f(\theta)|$ was obtained from given directional spectra $S_{\mathrm{SS}}(f,\theta)$ and $S^F_{\mathrm{IG}}(f,\theta)$, and the argument of $dA^{(1)}_f(\theta)$ was given randomly from $-\pi$ to π. $\xi^{(2)}_{n,\mathrm{IG}}$ was computed based on Equation 7 assuming that the second-order IG waves are generated only by coupling of two SS components. Therefore, synthetic data were generated solely from given $S_{\mathrm{SS}}(f,\theta)$ and $S^F_{\mathrm{IG}}(f,\theta)$.

$S_{\mathrm{SS}}(f,\theta)$ was determined as $E_{\mathrm{SS}}(f)D_{\mathrm{SS}}(\theta)$: Here, $E_{\mathrm{SS}}(f)$ was given by JONSWAP spectra with different significant wave height H_S and peak frequency f_p, and $D_{\mathrm{SS}}(\theta)$ was represented by $D_0\cos^{30}\left(\frac{\theta}{2}\right)$ with a peak direction of 0°. D_0 is a normalizing factor to satisfy $\int D_{\mathrm{SS}}d\theta = 1$. Similarly, S^F_{IG} was given by $E^F_{\mathrm{IG}}(f)D^F_{\mathrm{IG}}(\theta)$. Here, $E^F_{\mathrm{IG}}(f)$ was determined by the following empirical formula by Ardhuin et al. (2014), which was designed to give an empirical source of FIG waves to spectral wave models:

$$E^F_{\mathrm{IG}}(f) = 1.2\alpha_1^2\frac{kg^2}{c_g\omega}\left(\frac{1}{4}H_{m0}T^2_{m0,-2}\right)^2\frac{1}{\Delta_f}\min(1, 0.015/f)^{1.5}. \tag{12}$$

in which c_g is the group velocity, H_{m0} is the significant wave height, $T_{m0,-2}$ is the mean wave period, and Δ_f is controlled such that the integral of $\min(1, 0.015/f)^{1.5}/\Delta_f$ becomes unity. The coefficient α_1 was set to be $8\times10^{-4}\ \mathrm{s}^{-1}$ based on our in-situ data shown later.

Three types of numerical experiments were carried out by changing $D^F_{\mathrm{IG}}(\theta)$: (a) Unimodal case, (b) Bimodal case, and (c) Isotropic case. Table 1 summarizes the cases. In the unimodal case, $D^F_{\mathrm{IG}}(\theta)$ was represented by

$$D^F_{\mathrm{IG}}(\theta) = D_0\cos^{m_{\mathrm{IG}}}\left(\frac{\theta-\theta_{p,\mathrm{IG}}}{2}\right) \tag{13}$$

in which $\theta_{p,\mathrm{IG}}$ indicates the peak direction of FIG waves and m_{IG} controls the width of the directional distribution. For this case, $H_S, \theta_{p,\mathrm{IG}}, m_{\mathrm{IG}}$ were changed. In the bimodal case, $D^F_{\mathrm{IG}}(\theta)$ was given by a summation of primary and secondary unimodal directional distributions as

$$D^F_{\mathrm{IG}}(\theta) = D_0\left[\cos^{m_{\mathrm{IG}}}\left(\frac{\theta-\theta_{p1,\mathrm{IG}}}{2}\right) + \frac{1}{2}\cos^{m_{\mathrm{IG}}}\left(\frac{\theta-\theta_{p2,\mathrm{IG}}}{2}\right)\right]. \tag{14}$$

In the bimodal case, different pairs of $\theta_{p1,\mathrm{IG}}$ and $\theta_{p2,\mathrm{IG}}$ were tested for different m_{IG}. Finally, the isotropic case assumes a constant energy distribution over all directions and gives $D^F_{\mathrm{IG}}(\theta)$ as

$$D^F_{\mathrm{IG}}(\theta) = \frac{1}{2\pi}. \tag{15}$$

This is the assumption made by Ardhuin et al. (2014) and implemented in wave hindcasting models such as WAVEWATCH III (The WAVEWATCH III Development Group, 2016) or SWAN (Booij et al., 1999).

In all cases, the resolution of given spectra was set to be 0.0002 Hz in frequency and 5° in direction. In this method, two components of same frequencies and different directions always have a fixed phase difference in a single synthetic data set. The phase difference is determined by the initially given arguments of $dA^{(1)}_f(\theta)$, and as a result $\langle dA^{(1)*}_f(\theta')\,dA^{(1)}_f(\theta)\rangle = 0$ is not satisfied (Miles & Funke, 1989). Therefore, the assumption of Gaussian wave fields does not hold, and cross-spectra will be contaminated. In order to prevent this undesired coherence,

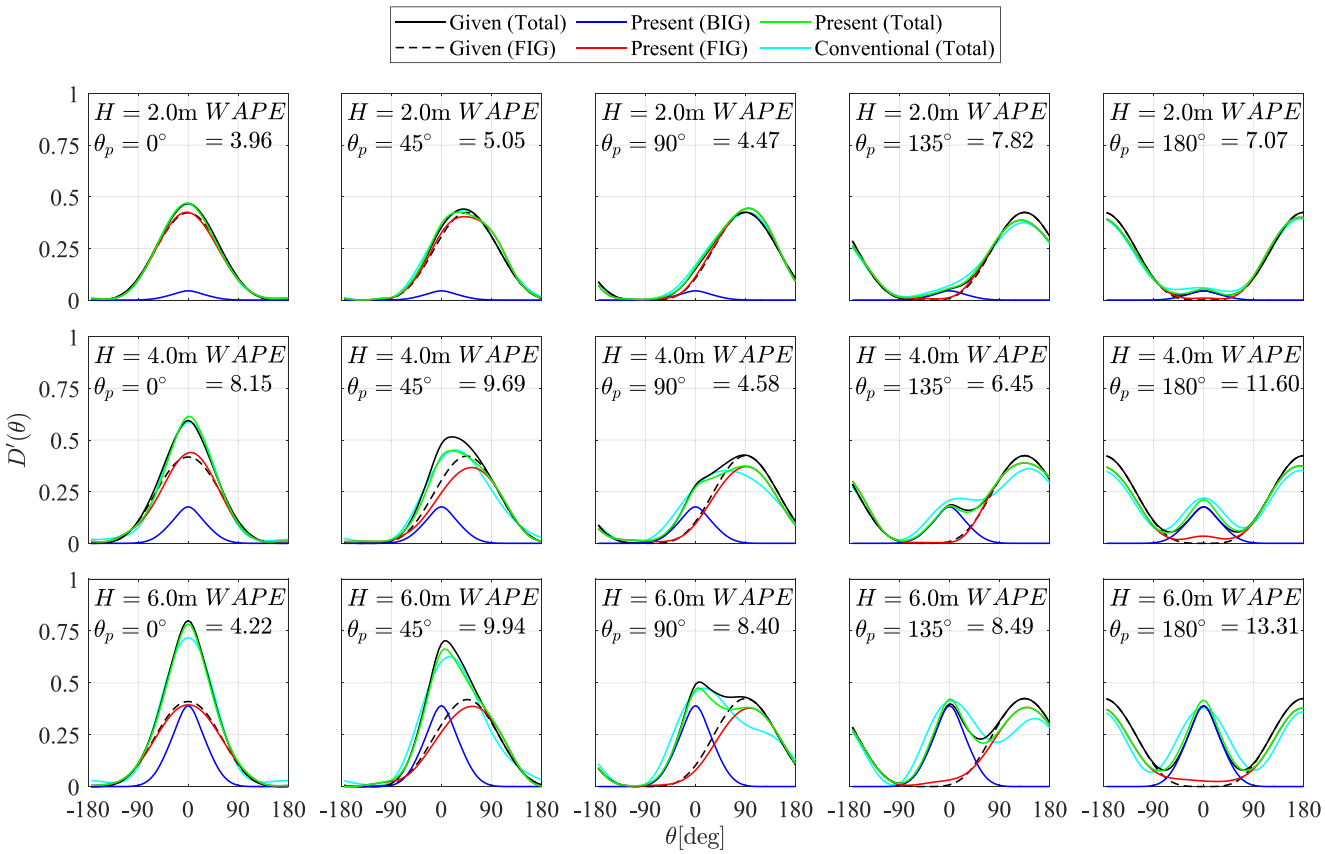

Figure 3. Results of numerical experiments: Unimodal cases ($m_{\mathrm{IG}} = 4$). The light blue lines indicate results computed by the conventional method relying on linear wave theory. The red, blue, and green lines correspond to $S^F_{\mathrm{IG}}(f,\theta)$, $S^B_{\mathrm{IG}}(f,\theta)$, and $S^F_{\mathrm{IG}} + S^B_{\mathrm{IG}}$ computed by the present method, respectively.

averaged cross-spectra were computed from 10 different signals with a length of 2048 s, which were generated by giving random initial arguments to $dA^{(1)}_f(\theta)$ in every case.

4. Results

4.1. Numerical Experiments

In the numerical experiments, cross-spectra among wave data $(\eta, U_{M,N}, p)$ were estimated with 50% overlapping Hanning windows of 256 s. The directional resolution was 5°. In order to demonstrate that $S^F_{\mathrm{IG}}(f,\theta)$ can be reconstructed by $\Phi^F_{mn}\left(= \Phi_{mn} - \Phi^B_{mn}\right)$, Φ^B_{mn} was computed from given $S_{\mathrm{SS}}(f,\theta)$. Note that we also applied $S_{\mathrm{SS}}(f,\theta)$ estimated from synthetic wave signals, but similar results were obtained owing to the good performance of the reconstruction method, as previously confirmed by Fujiki et al. (2017). The effects of estimation error of $S_{\mathrm{SS}}(f,\theta)$ can be found in Supporting Information S1. To demonstrate the performance quantitatively, an accuracy indicator named WAPE was computed following Oltman-Shay and Guza (1984) from given and estimated directional distributions of FIG waves, D^G_{IG} and D^F_{IG}, as

$$\mathrm{WAPE} = 100 \times \int |D^G_{\mathrm{IG}} - D^F_{\mathrm{IG}}| d\theta \tag{16}$$

Normalized directional distributions $D'(\theta)$, defined as $\int S(f,\theta)df / \int E_{\mathrm{IG}}(f)df$, of the unimodal cases ($m_{\mathrm{IG}} = 4$) are shown in Figure 3. Here, E_{IG} is total IG wave energy. As seen in this figure, very good agreement between the given and estimated FIG wave spectra can be confirmed in every case (WAPE < 15%), including cases of $H_s = 2$ m where BIG wave energy is small and extreme cases ($H_s = 6$ m) where BIG wave energy is comparable with FIG wave energy. In particular, the present method precisely captured the magnitude and location of the

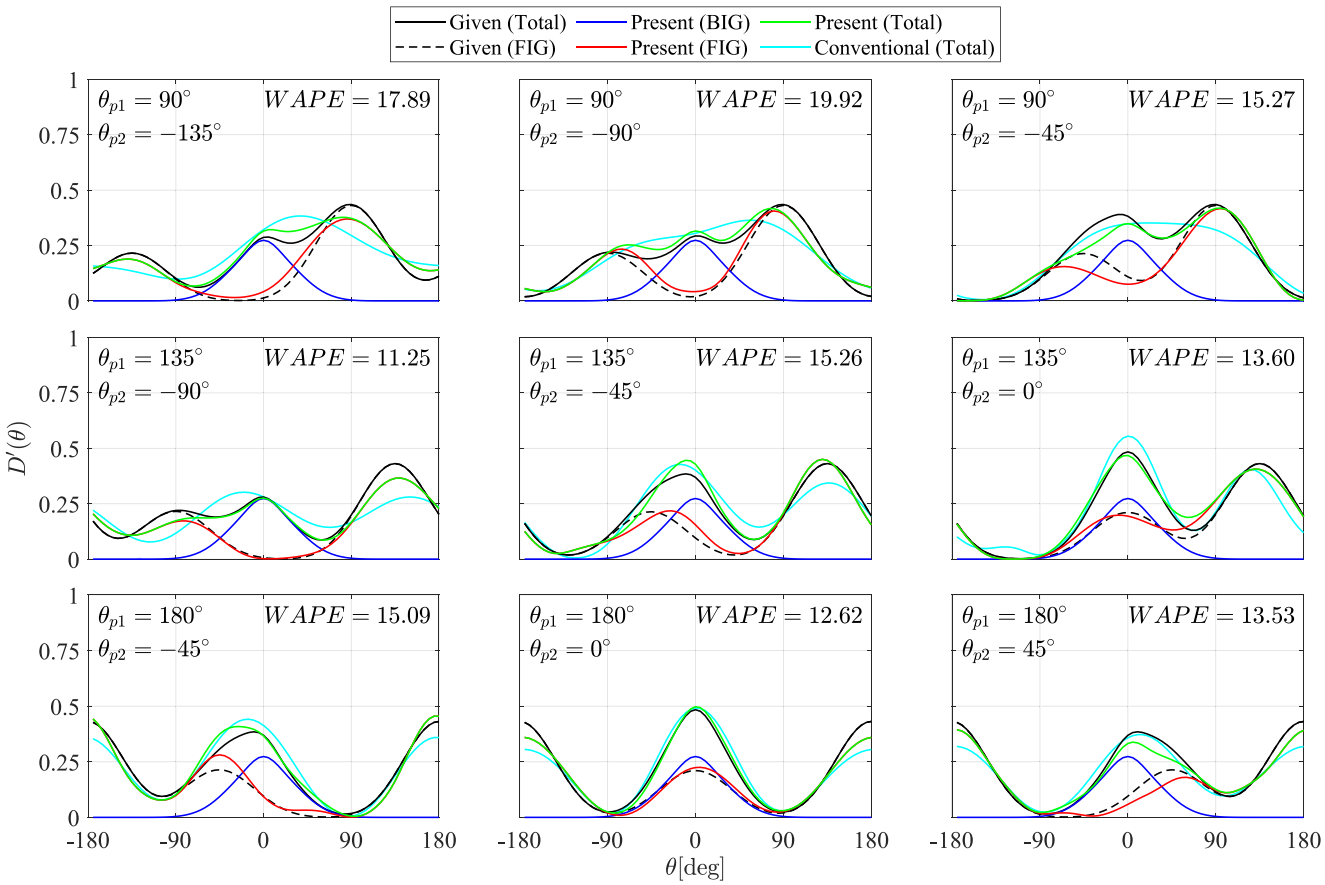

Figure 4. Results of numerical experiments: Bimodal cases ($m_{\mathrm{IG}} = 10$).

directional peaks of FIG waves, whereas the conventional method failed to detect directional peaks of both BIG and FIG waves in some extreme cases.

The superiority of the present method is more apparent in the bimodal cases ($m_{\mathrm{IG}} = 10$) shown in Figure 4. The conventional method could not detect the secondary spectral peaks due to the composition with the BIG wave spectra. Furthermore, it could not reproduce the primary peaks precisely in some cases (e.g., cases of $(\theta_{p1}, \theta_{p2}) = (90°, -90°), (135°, -90°)$). In contrast, the present method succeeded in reproducing the given spectral shape including the secondary peaks of FIG waves in all cases, though some deviations occurred (WAPE < 20%). Similar results were obtained in the cases with other m_{IG} (see Supporting Information S1), confirming the good estimation skill of the present method for all considered directional widths.

Finally, Figure 5 shows the results of the isotropic cases. As seen in this figure, the conventional method produced false spectral peaks at $\theta = \pm 180°$ in some cases, in particular in energetic conditions, because of the different transfer functions of FIG and BIG waves. Therefore, the isotropic directional distributions could not be reproduced at all. In contrast, the present method successfully reproduced an almost uniform spectral shape, in particular in the cases of $f_p = 0.08$ Hz (WAPE < 10%). Errors were largest for $f_p = 0.14$ Hz, possibly because $E^F_{\mathrm{IG}}/E_{\mathrm{IG}}$ decreases following an increase in f_p in the present settings. The estimation error of Φ^F_{mn}, which are equal to that of Φ_{mn} here, could be relatively large.

The numerical experiments using synthetic data showed that the proposed method was generally able to accurately reproduce the directional distributions of FIG waves. They also confirmed the superiority of the present method over the conventional method. Even though the current numerical experiments were conducted under idealized conditions and thus the reliability of this method in the field cannot be asserted solely from these results,

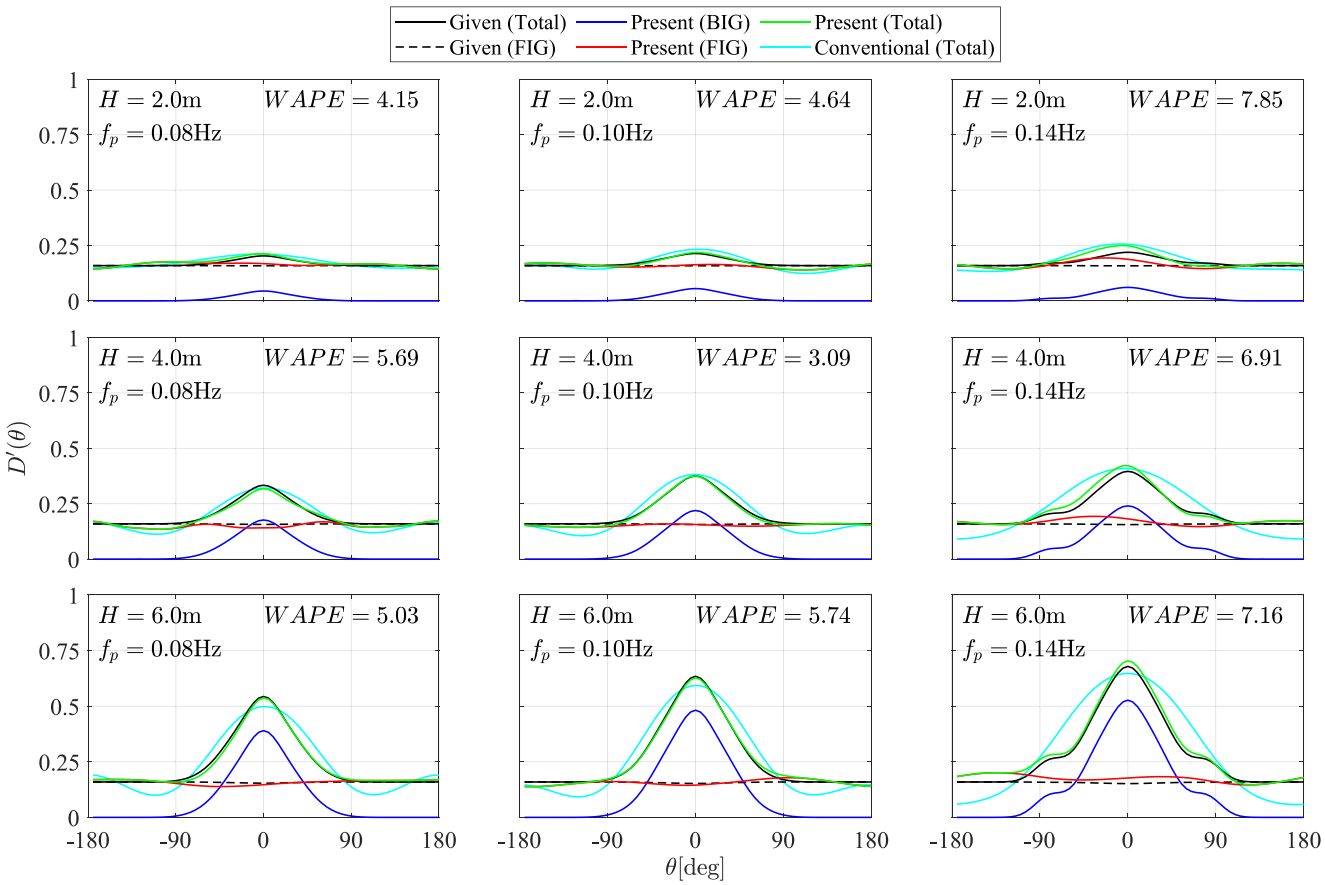

Figure 5. Results of numerical experiments: Isotropic cases.

it was demonstrated that the present method is applicable to discuss directional distributions of FIG waves in the intermediate depth as long as the magnitude, direction, and phase of BIG waves follow H62.

4.2. Observed Bound/Free IG Wave Directional Spectra

Here, results of field application of the present method to the in-situ data at 207 and 106 are described. In this study, the top 10 stormy days were selected from the in-situ data during six years from 2015 to 2020 at each point, and the present method was applied to 2-hr wave data $(\eta, U_{M,N}, p)$ around a peak of observed wave heights within each day. The spectral estimation was conducted with the same settings as in the numerical experiments.

At first, frequency distributions of the observed FIG waves $E^F_{\mathrm{IG}}(f) = \int S^F_{\mathrm{IG}}(f,\theta)d\theta$ are discussed. The empirical formula by Ardhuin et al. (2014), Equation 12, can be divided into two parts: $1.2\alpha_1^2 \frac{kg^2}{c_g\omega}\left(\frac{1}{4}H_{m0}T^2_{m0,-2}\right)^2$ which determines the magnitude of each frequency component, and $\frac{1}{\Delta_f}\min(1, 0.015/f)^{1.5}$ which gives the universal frequency distribution of IG waves. Based on this formula, Figure 6 shows observed $E^F_{\mathrm{IG}}(f)$ normalized by the former term, and the universal frequency distribution is shown by the black solid line. Here, α_1 was given as 8×10^{-4} s^{-1} which gave the best agreement at both observatories. Note that $\frac{kg^2}{c_g\omega}$ is a frequency-dependent parameter, but it does not significantly differ within the IG frequency band (less than 10% in these cases) and the normalization does not modify the original spectral shape.

At both stations, the observed frequency distribution showed significant scatter around the mean (in particular at 106), but the mean shows similar tendency with the empirical formula (Figure 6). Low frequency components around 0.01 Hz were dominant. The present result suggests that the equation is somehow applicable to predict

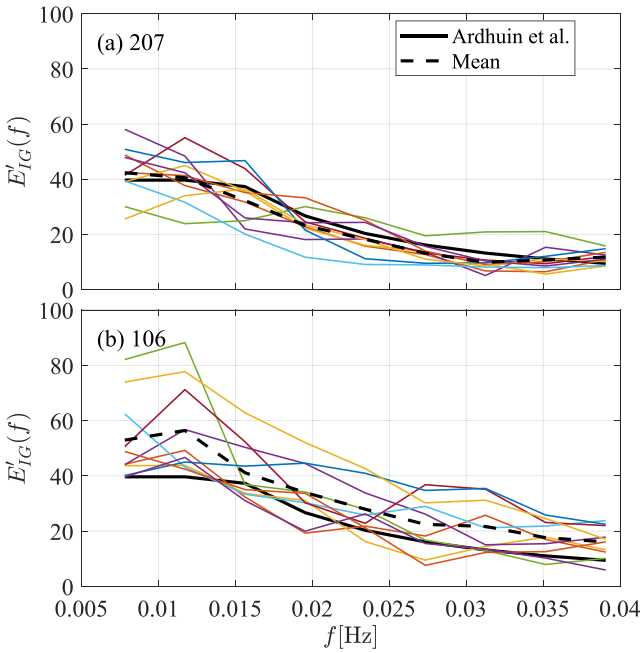

Figure 6. Normalized frequency distributions of FIG waves at (a) 207 and (b)106. Colored lines correspond to each case, and the black dashed line shows their mean. The black solid line is $\frac{1}{\Delta_f}\min(1, 0.015/f)^{1.5}$ following the empirical formula.

frequency distributions of FIG waves, though the determination of α_1 requires local tuning.

Next, Figures 7 and 8 show estimated directional distributions of FIG/BIG waves of the 10 stormy cases at 207 and 106, respectively. Here, the wave direction in the geographical coordinates θ is converted to that in the local coordinates θ': $0° < \theta' < 180°$ corresponds to seaward components and $-180° < \theta' < 0°$ to shoreward components. The angle increases in the anti-clockwise direction.

At 207, nearly isotropic directional distributions were estimated by the conventional method in some cases (e.g., Case 1, 2, 6) (Figure 7). However, the present method yielded clear directional peaks of BIG waves at around $-90°$ corresponding to the shore-normal direction and ones of FIG waves at around 90° corresponding to the seaward direction. White dots in the lower panels indicate estimated directional peaks of FIG wave energy originated from the reflection of incident BIG waves at the shore (see Herbers, Elgar, and Guza (1995) for the method). As seen here, each observed directional peak of each frequency component roughly agreed well with the estimation, though the observed peaks occurred at slightly larger θ'. These results suggest that FIG waves observed at 207 seemed to be dominated by the reflection from the alongshore seawall, not by the reflection from the breakwater nor incoming components from the remote sources. The secondary peaks appearing at 0° in some cases seemed to be generated by the reflection from the breakwater.

At 106, different characteristics were found. As seen in Figure 8, while spectral peaks corresponding to the reflection from the shore could not be confirmed in most cases, clear spectral peaks were generated near $\theta' = \pm 180°$, which correspond to alongshore propagating components from right to left facing the sea. On the right of the observatory, a long breakwater is located and the alongshore components seemed to be the reflected IG waves from the breakwater. Additionally, secondary spectral peaks were confirmed around $\theta' = 0°$ in some cases. The directional distributions estimated by the conventional method yielded similar spectral shapes with the ones of total IG waves given by the present method, but the spectral peaks of FIG waves were estimated to be smaller by the former and it missed the secondary spectral peaks (e.g., Case 5, 9).

At both observatories, FIG wave energy accounted for more than the half of the total IG energy in all cases. The empirical formula Equation 12 represented the frequency distributions of FIG waves well, but it was found that the assumption of the isotropic directional distribution is not valid, at least, at the present observatories. Although the directional distributions of FIG waves were more gradual than the ones of BIG waves, the present method showed clear directional peaks in the FIG directional distributions. The conventional method was not always able to recover these peaks, illustrating that BIG waves can have significant effects on the estimations by the conventional method. Although true FIG wave spectra are not available prohibiting a direct validation of the proposed method, the FIG directional distributions appear largely consistent with reflection of FIG waves from nearshore coasts and structures (which will be discussed in more detail in Section 5.1).

5. Discussion

5.1. Reflection From Shore and Coastal Structures

In the previous section, seaward propagating waves were found to dominate the FIG directional distribution at 207 whereas alongshore propagating components dominated at 106. We conducted additional numerical simulations employing XBeach in surfbeat mode (Roelvink et al., 2009) to understand these FIG directional distributions. XBeach solves the spatial and temporal evolution of IG waves using nonlinear shallow water equations with SS-wave forcing from wave-action balance equations. In this analysis, the wave fields in Case 6 were computed by XBeach as FIG directional distributions were markedly different at both observatories (see Figures 7 and 8).

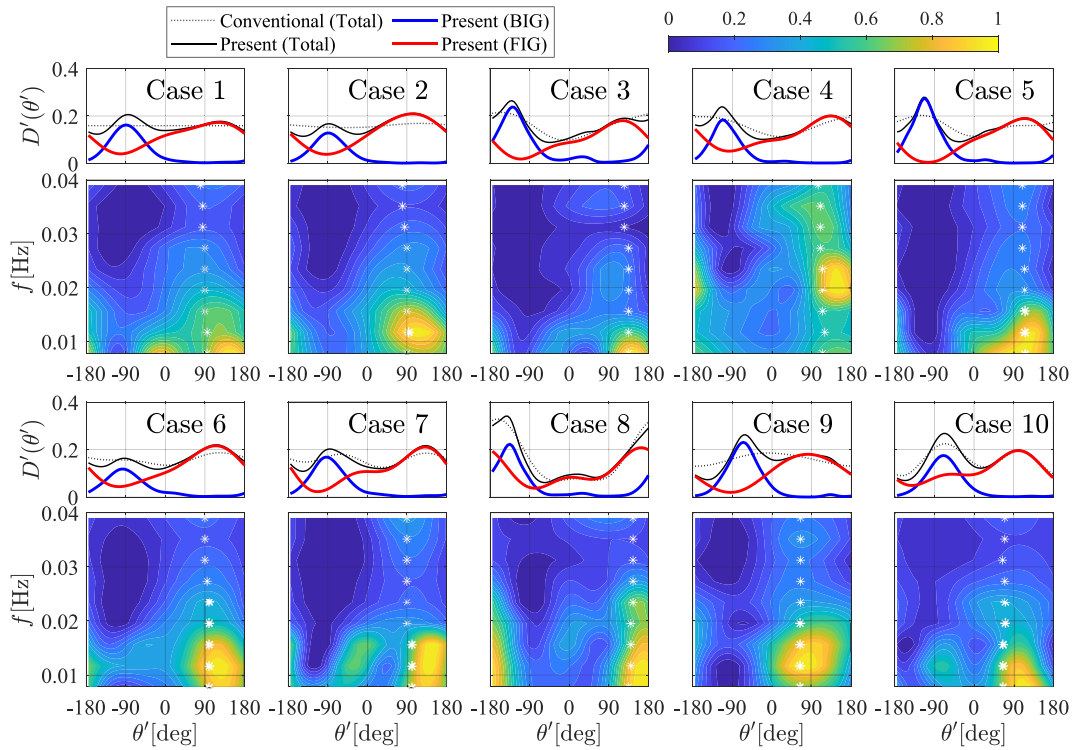

Figure 7. Directional spectra of infragravity (IG) waves at 207. (Upper panels) Normalized directional distributions $D'(\theta')$. Black dotted lines show the directional distributions of total IG waves obtained by the conventional method. The black solid lines show the ones by the present method computed as $S^B_{\mathrm{IG}}(f,\theta') + S^F_{\mathrm{IG}}(f,\theta')$. (Lower panels) Directional spectra of FIG waves. Each directional spectrum is normalized by the maximum value within the domain. White dots show predicted peak wave directions of outgoing IG waves reflected at the shore following Herbers, Elgar, and Guza (1995).

The model domain was set around each observatory and its offshore boundary was located in a relatively mildly sloping area deeper than 40 m (see Figures 2b and 2c for the entire domain and Figures 9a and 9d for the enlarged view around each observatory). The domain was discretized with a uniform grid in the alongshore direction (20 m) and varying grid in the cross-shore direction (∼20 m at offshore to ∼3 m in shallow water). The grids resolve a wavelength of the dominant IG frequency component (<0.02 Hz) by more than 50 points in the cross-shore direction and 25 points in the alongshore direction (at the observatory). The time step of about 0.1 s was internally determined. The model was forced at the offshore boundary with observed SS directional spectra with similar mean directions in both cases (−91° at 207 and −85° at 106). The radiation condition was applied at the lateral boundary. The propagation of SS wave energy was computed along the mean wave direction following Roelvink et al. (2018) to avoid a non-realistic decrease in wave groupiness of refracted incident SS waves. Default values were used for other model settings. Simulations were run for a duration of 140 min including 20 min spin-up time, which provides 120 min of model output for further analysis of the IG wave fields. To understand the influence of the breakwaters on FIG wave directional distributions, we ran an additional simulation at both sites for a domain excluding the breakwaters.

From the model results, directional wavenumber spectra $F(f,k,\theta)$ were estimated following Capon (1969). The method does not assume a unique dispersion relation, and thus directional distributions of IG waves can be computed without distinguishing between FIG and BIG waves from water level changes at multiple points. $F(f,k,\theta)$ was computed from the modeled water level signals at the observatory and 16 surrounding grid points located at a distance of about $0.2\lambda_L$ from the observatory (λ_L is a wavelength of FIG waves with frequency of f Hz using linear wave theory). Note that this method requires a dedicated coherent spatial instrument array in the field that is typically not feasible.

Figures 9b and 9e show the directional wavenumber spectra at 0.012 Hz (the closest bin to the observed peak IG frequency) in which the wavenumber axes are normalized by $k_L = 2\pi/\lambda_L$. In the figure, circles corresponding

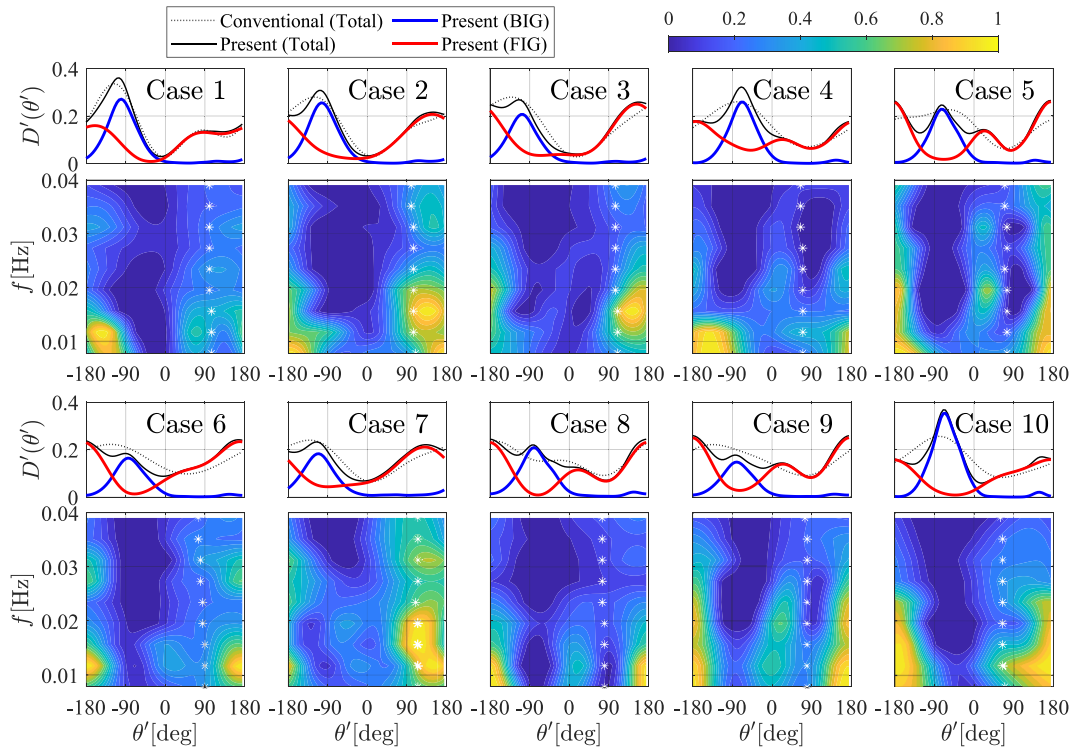

Figure 8. Directional spectra of infragravity (IG) waves at 106. Details are same with Figure 7.

to $k = k_L$ and $k = k_{NL}$ are shown. k_{NL} is an estimated wavenumber of BIG waves given as $2\pi f/c_g$ with the group velocity of the peak SS frequency component c_g and $f = 0.012$ Hz. At both observatories, spectral peaks of shoreward components can be confirmed at $(k_x, k_y) \cong (0, -k_{NL})$ corresponding to incident BIG waves. On the other hand, spectral peaks of FIG waves ($k \cong k_L$) appear at different (k_x, k_y) at both observatories. The primary directional peak of FIG waves around $(0, k_L)$ is offshore directed at 207, whereas the primary peak around $(-k_L, 0)$ at 106 is alongshore as also discussed before (Section 4.2).

The different directional peaks are evident in the directional distributions of IG waves. Modeled directional distributions computed as $\int_f \int_k F(f, k, \theta) dk df$ are compared with the observed ones computed by the present method, $\int_f S^F_{\mathrm{IG}} + S^B_{\mathrm{IG}} df$, in Figures 9c and 9f. Even though the total IG wave energy was underestimated by the model, the modeled directional distributions agree with the observed distributions; shoreward propagating BIG waves ($\theta' = -90°$) at both sites, offshore directed FIG waves ($\theta' = 90°$) at 207, and alongshore propagating FIG waves ($\theta' = \pm 180°$) at 106. Spectral peaks of shoreward propagating BIG waves were overestimated possibly because $F(f, k, \theta)$ was estimated from a set of points where still water depth differs by a few meters.

Furthermore, XBeach simulations excluding the breakwaters provided additional insight into the influence of these coastal structures on the IG wave field. Excluding the breakwater did not affect the directional distribution significantly at 207, whereas the exclusion resulted in a clear decrease of the alongshore IG components at 106. These results indicate that FIG waves reflected at the shore are dominant at 207 whereas the FIG waves are dominated by reflected components from the breakwater at 106.

Finally, spatially different contributions of the breakwaters are shown in Figures 9a and 9d. Here, spectral wave heights of IG waves in the case with/without the breakwaters are computed as H_{IG} and $H_{\mathrm{IG},0}$ respectively, and $\frac{H_{\mathrm{IG}}}{H_{\mathrm{IG},0}} - 1$ is shown. The increase in IG wave heights owing to the breakwater is more evident at 106 than 207, and it reaches up to 20% at the seaward of the breakwater including the observatory location. The increase is negligibly small in shallow water (<10 m), possibly because incident BIG waves are dominant, except at the foot of the breakwater at 106 where alongshore propagating FIG waves locally increase IG wave heights by about 20%.

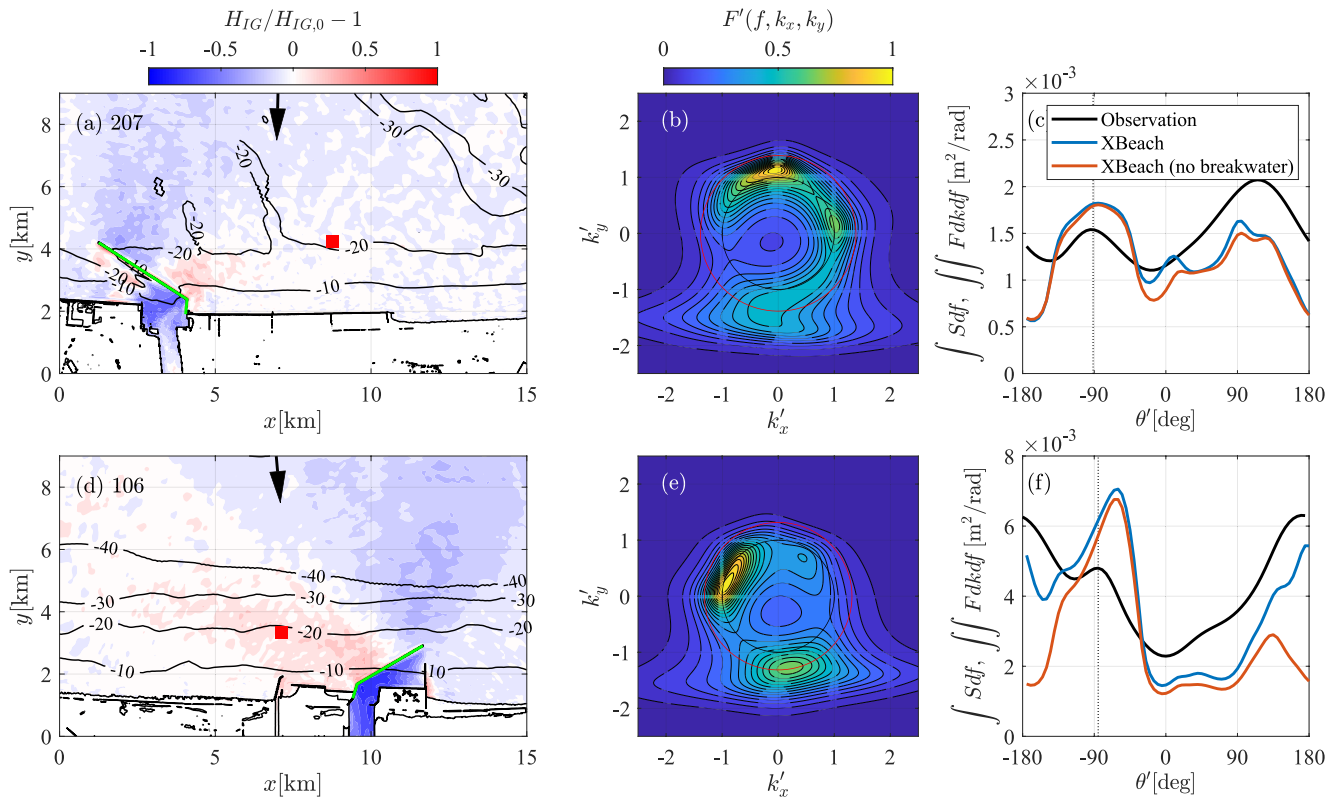

Figure 9. Results of numerical modeling using XBeach. (Left) Enlarged map around observatory and the rate of increase in infragravity (IG) wave heights owing to the presence of the breakwater (shown in green). The black arrow shows the mean direction of incident SS wave θ_m. (Middle) Normalized directional wavenumber spectrum for 0.012 Hz estimated at the observatory. The black/red circles show wavenumbers of FIG/BIG waves, respectively. (Right) Modeled/observed directional distributions of IG waves. The dotted line indicates θ_m. (a–c) At 207. (d–f) At 106.

Overall, these results suggest that local intensity of FIG waves and their directional distributions are highly affected by the regional coastal topography and the presence of coastal structures which control the dominant directions of reflected IG waves.

5.2. Validity of H62 and Applicability of the Present Method

The fundamental premise of the present method is that the magnitude and the transfer functions of BIG waves follow H62. However, H62 is formally not valid on a sloping bottom. Therefore, deviations of the coupling coefficient Ω and the transfer function $H^{(2)}_{n,f}$ from H62 will increase the estimation error of this method. To understand the validity of the underlying coupling coefficient Ω and transfer functions $H^{(2)}_{n,f}$ of the proposed reconstruction method, we apply bispectral analysis following a similar approach to Herbers et al. (1994).

A cross-bispectrum is computed from the coupling of a triad of waves with different frequencies,

$$B_{X,Y,Z}(f, f_1) = \langle \frac{dX_f dY_{f_1} dZ^*_{f_2}}{df^2} \rangle, \tag{17}$$

where dX_f indicates the Fourier amplitude of the f- Hz component of signal X and $f_2 = f + f_1$. If the second-order SS waves are negligible, the cross-bispectrum of (ξ_n, η, η) with f in the IG frequency range can be computed as

$$B_{\xi_n,\eta,\eta}(f, f_1) = \langle \frac{\int_{f_1=0}^{\infty} \int_{\theta_1} \int_{\theta_2} H^{(2)}_{n,f} \exp(i\Delta \boldsymbol{k} \cdot \boldsymbol{x_n}) \, dA^{(2)}_f(f_1, \theta_1, \theta_2) \int_{\theta_1} dA^{(1)}_{f_1} \int_{\theta_2} dA^{(1)*}_{f_2}}{df^2} \rangle. \tag{18}$$

Here, the first-order term for IG waves is neglected because the cross-bispectrum among $\left(\xi_n^{(1)}, \eta, \eta\right)$ vanishes. Considering a Gaussian wave field in a similar manner to the derivation of Equation 9 results in the following equation:

$$2B_{\xi_n,\eta,\eta}(f, f_1) = \int_{\theta_1}\int_{\theta_2} \widehat{H}_{n,f}^{(2)} \exp\left(i\widehat{\Delta \boldsymbol{k}} \cdot \boldsymbol{x_n}\right) S^{(1)}(f_1, \theta_1) S^{(1)}(f_2, \theta_2) \widehat{\Omega} d\theta_1 d\theta_2. \tag{19}$$

Here, ^ on $\Delta \boldsymbol{k}$, Ω, and $H_{n,f}^{(2)}$ is added to highlight that they are true values in the field which may deviate from H62. The right hand of the equation can be estimated from measured $S_{\mathrm{SS}}(f, \theta)$ with Ω and $H_{n,f}^{(2)}$ based on H62. Therefore, the validity of Ω and $H_{n,f}^{(2)}$ can be evaluated indirectly by comparing the cross-bispectrum computed from the measured wave signals $B_{\xi_n,\eta,\eta}$ and the one estimated from the measured SS directional spectrum with Ω and $H_{n,f}^{(2)}$ from H62. We test $B_{\eta,\eta,\eta}(f, f_1)$ for the evaluation of Ω as $H_{\eta,f}^{(2)} = 1$ and $B_{U_{M,N},\eta,\eta}(f, f_1)$ for the transfer functions of $U_{M,N}^{(2)}$. Here, $\Delta \boldsymbol{k} \cdot \boldsymbol{x_n}$ is negligibly small because of the long IG wavelengths relative to the small distances $|\boldsymbol{x_n}|$ between the DWM beams. At water depth of 25 m for example, $\Delta \boldsymbol{k} \cdot \boldsymbol{x_n}$ is about 0.03π for the velocity measurement at the upper layer (15 m from the bottom) when considering the colinear interaction between 0.08 and 0.10 Hz wave components. Furthermore, $H_{U_{M,N},f}^{(2)}$ is given by $H_{u,f}^{(2)} \sin\alpha \cos(\theta_b - \beta_M) + H_{w,f}^{(2)} \cos\alpha$, in which θ_b is the wave direction of BIG waves. Therefore, the real and imaginary parts of $B_{U_{M,N},\eta,\eta}(f, f_1)$ are dominantly determined by $\hat{H}_{u,f}^{(2)}$ and $\hat{H}_{w,f}^{(2)}$ respectively, considering that the former is a real number and the latter is a pure imaginary number (see Supporting Information S2). As a result, the real and imaginary parts of $B_{U_{M,N},\eta,\eta}(f, f_1)$ can be used for the evaluation of $H_{u,f}^{(2)}$ and $H_{w,f}^{(2)}$, respectively.

To achieve quantitative evaluation of the coupling coefficient and transfer functions, we integrated bispectra as follows:

$$I_B = \int\int 2B_{\xi_n,\eta,\eta}(f, f_1)\, df_1 df, \tag{20a}$$

$$I_S = \int\int\int\int H_{n,f}^{(2)} S^{(1)}(f_1, \theta_1) S^{(1)}(f_2, \theta_1) \Omega d\theta_1 d\theta_2 df_1 df. \tag{20b}$$

Bispectra were integrated to reduce the scattering owing to errors in their estimation (e.g., Herbers et al., 1994). At both observatories 207 and 106, 3h-segments from the top 100 stormy days were chosen for the analysis. A data set was considered unreliable and discarded when the occasional missing of measurement signals reduced the degrees of freedom for the bispectral estimation to less than 250, at which the 95% significant bicoherence is less than 0.15.

Figures 10a and 10b show the results of $B_{\eta,\eta,\eta}(f, f_1)$ to evaluate the validity of Ω. The theoretical prediction I_S agreed well with the real part of I_B, $\Re[I_B]$ (Figure 10a). The slight underestimation of $\Re[I_B]$ can be explained by the argument of I_B that is shown in Figure 10b. When the directional spreading of incident waves is narrow, Ω is a negative real number. In that case, the biphase (the argument of $B_{\eta,\eta,\eta}(f, f_1)$) is $\pm\pi$, and thus the argument of I_B is expected to be $\pm\pi$. Most instances agreed with this $\pm\pi$ biphase, but the slight deviations from $\pm\pi$ in the third quadrant can be observed, in particular for larger $|I_B|$. The deviations indicate that the BIG waves were slightly delayed compared to H62's equilibrium response. Such a phase lag has been previously observed for waves propagating over a sloping bottom (e.g., Janssen et al., 2003; Matsuba et al., 2021b; Moura & Baldock, 2017). Deviations from the equilibrium response occurred for energetic conditions, but are relatively small ($\sim 0.1\pi$) compared with the previous studies which showed deviations exceeding 0.25π (e.g., Battjes et al., 2004). Overall, the observed bispectral quantities were well predicted by Equation 19, which demonstrates the validity of Ω from H62 for the conditions of waves and topography considered in this study.

Next, the results of $B_{U_{M,1},\eta,\eta}(f, f_1)$ are shown in Figures 10c and 10d to evaluate the validity of $H_{U_{M,1},f}^{(2)}$ from H62. Here, real and imaginary parts of I_B and I_S are compared, which are dominated by $H_{u,f}^{(2)}$ and $H_{w,f}^{(2)}$ respectively. I_S showed good agreement with I_B regardless of measurement angles and observation points (Figures 10c and 10d). Slight overestimation of the imaginary part of I_B, $\Im[I_B]$, possibly occurred owing to the forementioned delay of BIG waves. This could also be related to a coupling among higher frequency components, for whom $H_{w,f}^{(2)}$ is relatively large (see Figure 1), whereas their interactions might be weaker as they might not have reached equilibrium

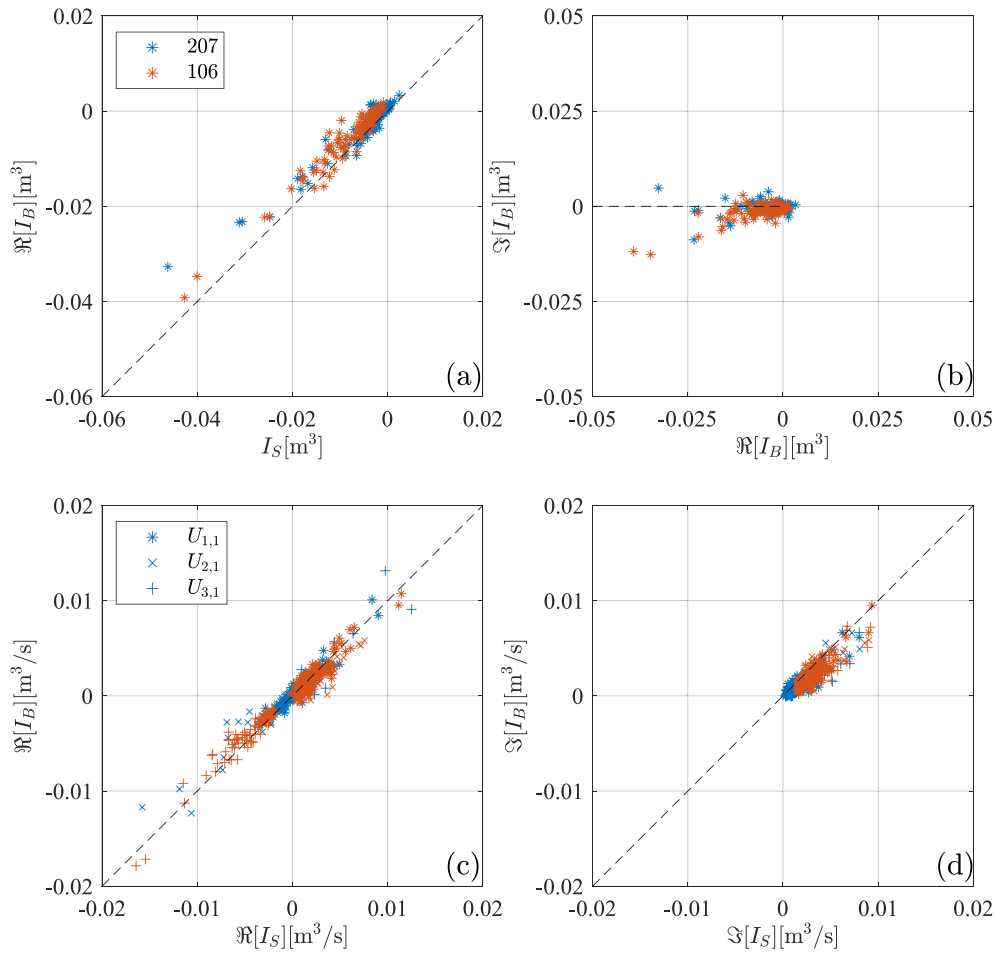

Figure 10. Results of bispectral analysis. (a), (b) Evaluation of Ω focusing on $B_{\eta,\eta,\eta}$. (a) I_S versus $\Re\,[I_B]$. Note that I_S is a real number. (b) $\Re\,[I_B]$ versus $\Im\,[I_B]$. (c), (d) Evaluation of $H^{(2)}_{u,f}$ and $H^{(2)}_{w,f}$ focusing on $B_{U_{M,1},\eta,\eta}$. (c) $\Re\,[I_S]$ versus $\Re\,[I_B]$. (d) $\Im\,[I_S]$ versus $\Im\,[I_B]$. The dashed black lines show agreement of observation with H62.

conditions yet due to their limited wave age. Nonetheless, I_S agreed well with I_B, which suggests that the transfer functions derived from H62 were valid for the wave conditions of the present data set.

The bispectral analysis confirmed that the hydrodynamics of BIG waves at the present observatories (located at the depth of ~25 m) can be well represented by H62. However, as also suggested by numerous previous studies, H62 will not be applicable to nearshore waves on a sloping bottom. To further discuss the deviations from H62 and the applicability of the present method in other situations, we employed a semi-analytical solution of wave-group forced IG waves proposed by Guérin et al. (2019) based on Schäffer (1993). The solution is derived from linear shallow water equations with the forcing term due to radiation stress on a uniform sloping bottom. Based on the solution, the magnitude and phases of IG waves were computed. By comparing them with the equilibrium solution of H62 for each depth, the deviation of IG wave height ($\hat{\Omega}/\Omega$) and the phase lag ($\Delta\phi$) from H62 was predicted for various IG frequencies f_{IG} (0.01, 0.02, and 0.03 Hz) and bottom slopes h_x (1/50, 1/100, 1/200, and 1/300). The peak SS frequency (0.08 Hz) and the wave height (5 m) were not varied. The deviation is minor up to 20 m depth ($\hat{\Omega}/\Omega > 0.9$ and $\Delta\phi < 0.1\,\pi$) on the mildly sloping bottoms (1/200, 1/300), but it is pronounced on the relatively steep bottom (1/50) in particular at lower frequency (Figure 11). The results could not be simplified by a non-dimensional parameter $\beta_s = \frac{h_x}{2\pi f_{\mathrm{IG}}}\sqrt{\frac{g}{h}}$ (not shown), but the present results agree well with the findings based on laboratory experiments by Battjes et al. (2004). Even though the local bottom slope at 106 is about 1/100 and the dominant IG frequency was 0.01 Hz in the present cases, relatively small deviation ($\Delta\phi < 0.1\,\pi$) was observed possibly because the seaward bottom profile is much milder (<1/200). The results

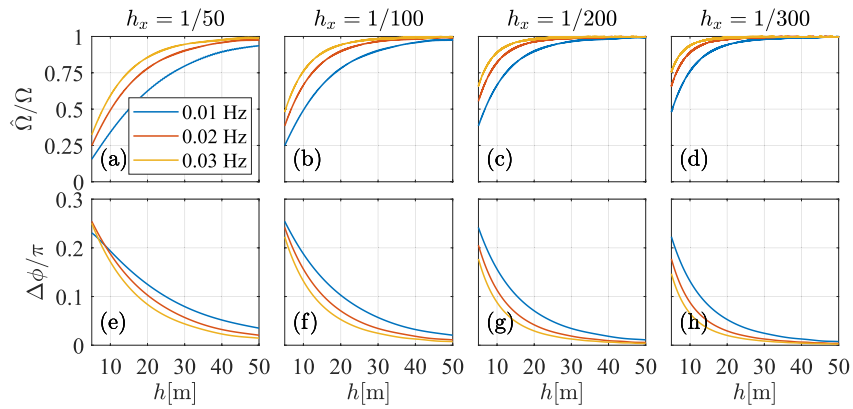

Figure 11. Deviation from H62 predicted by the analytical solution. (a–d) Relative IG wave heights to the equilibrium solution. (e–h) Phase lag of IG waves from wave groups.

suggest that the present reconstruction method based on H62 may fail to estimate the directions of FIG waves (particular for low frequency IG waves) on relatively steep (>1/100) and/or shallow (<20 m) points where H62 underestimates/overestimates magnitude of FIG/BIG waves. Conventional methods may be applicable in such conditions because $H^{(2)}_{n,f}/H^{(1)}_{n,f}$ gets close to unity in shallow water. Careful consideration is thus required to select the appropriate method to accurately reconstruct the IG wave directional spectra in the field.

6. Summary and Conclusions

Directional spectra of IG waves are generally estimated in the same way as SS waves, which inherently assumes that every wave component behaves as a (linear) first-order wave. However, this approach is problematic in intermediate water depths where the IG wave field is composed of free and bound wave components. This study proposed a new method to reconstruct the directional spectra of both FIG and BIG waves based on weakly nonlinear wave theory (H62). This method computes cross-spectra among BIG waves from the directional spectrum of SS waves based on H62, and they are used to obtain the cross-spectra among FIG waves, which is subsequently used to reconstruct the directional spectrum of FIG waves. The method was tested using synthetic data representing diverse directional distributions of FIG waves (ranging from unimodal to isotropic distributions). The proposed reconstruction method that accounts for the presence of (nonlinear) BIG waves was superior over conventional methods which rely on linear wave theory.

The new reconstruction method was applied to field data of energetic sea states in intermediate water depths. FIG wave directional distributions during stormy conditions were found to have clear directional peaks that could be explained by reflection of incoming IG waves at the shore and/or coastal structures. Furthermore, the validity of a nonlinear coupling coefficient and transfer functions of the underlying theory was confirmed using bispectral analysis for the intermediate water depths that were considered in this study. However, an analysis employing a semi-analytical solution of IG waves suggested that errors in the reconstruction increase in shallow water for low frequency IG waves on a steep profile, as the underlying theory breaks down for shoaling BIG waves.

Through this study, it was confirmed that the new reconstruction method significantly improves the reconstruction of IG wave directional spectra at the intermediate depth compared to conventional methods. In particular, the proposed method gives good estimation regardless of the shape of the directional distributions. The proposed method will help future studies to elucidate both magnitude and directions of FIG waves at intermediate depths. This will likely benefit further improvements of the boundary conditions of numerical models by including incident FIG waves in order to achieve accurate predictions of coastal disaster and morphological change.

Data Availability Statement

The measurement data at NOWPHAS observatories are provided by Ministry of Land, Infrastructure, Transport and Tourism, Japan (https://www.mlit.go.jp/kowan/nowphas/index_eng.html). The bathymetry data used in the numerical computations were generated from the M7000 series of seabed topography provided by Japan

Hydrographic Association (https://www.jha.or.jp/en/jha/business/b07.html). XBeach is available freely at https://oss.deltares.nl/web/xbeach/release-and-source. The other presented data and the source codes to reconstruct directional spectra of IG waves can be downloaded at https://doi.org/10.6084/m9.figshare.17157902.v1.

Acknowledgments
YM was supported by JSPS Oversea Fellowship. The authors thank Port and Harbour Bureau of the Ministry of Land, Infrastructure, Transport and Tourism, Japan, who shared the measurement data at NOWPHAS observatories. The authors thank Dr. Thomas Guérin, who kindly shared an original code to compute the semi-analytical solution.

References

Ardhuin, F., Rawat, A., & Aucan, J. (2014). A numerical model for free infragravity waves: Definition and validation at regional and global scales. *Ocean Modelling*, *77*, 20–32. https://doi.org/10.1016/j.ocemod.2014.02.006

Barstow, S. F., Bidlot, J.-R., Caires, S., Donelan, M. A., Drennan, W. M., Dupuis, H., et al. (2005). *Measuring and analysing the directional spectrum of ocean waves*. In D. Hauser, K. Kahma, H. Krogstad, S. Monbaliu, & S. L. et L. Wyatt (Eds.), COST Office. Retrieved from https://hal.archives-ouvertes.fr/hal-00529755

Battjes, J. A., Bakkenes, H. J., Janssen, T. T., & van Dongeren, A. R. (2004). Shoaling of subharmonic gravity waves. *Journal of Geophysical Research*, *109*(C2), C02009. https://doi.org/10.1029/2003JC001863

Battjes, J. A., & Stive, M. J. F. (1985). Calibration and verification of a dissipation model for random breaking waves. *Journal of Geophysical Research*, *90*(C5), 9159. https://doi.org/10.1029/JC090iC05p09159

Benoit, M., Frigaard, P., & Schaffer, H. A. (1997). Analyzing multidirectional wave spectra: A tentative classification of available methods. In *Proceedings of the 1997 IAHR conference* (pp. 131–158).

Bertin, X., de Bakker, A., van Dongeren, A., Coco, G., André, G., Ardhuin, F., et al. (2018). Infragravity waves: From driving mechanisms to impacts. *Earth-Science Reviews*, *177*(January), 774–799. https://doi.org/10.1016/j.earscirev.2018.01.002

Bertin, X., Martins, K., Bakker, A., Chataigner, T., Guérin, T., Coulombier, T., & Viron, O. (2020). Energy transfers and reflection of infragravity waves at a dissipative beach under storm waves. *Journal of Geophysical Research: Oceans*, *125*(5), 1–18. https://doi.org/10.1029/2019JC015714

Biésel, F. (1952). Equations générales au second ordre de la houle irrégulière. *La Houille Blanche*, *38*(3), 372–376. https://doi.org/10.1051/lhb/1952033

Booij, N., Ris, R. C., & Holthuijsen, L. H. (1999). A third-generation wave model for coastal regions: 1. Model description and validation. *Journal of Geophysical Research*, *104*(C4), 7649–7666. https://doi.org/10.1029/98JC02622

Capon, J. (1969). High-resolution frequency-wavenumber spectrum analysis. *Proceedings of the IEEE*, *57*(8), 1408–1418. https://doi.org/10.1109/PROC.1969.7278

Contardo, S., Lowe, R. J., Hansen, J. E., Rijnsdorp, D. P., Dufois, F., & Symonds, G. (2021). Free and forced components of shoaling long waves in the absence of short-wave breaking. *Journal of Physical Oceanography*, *51*(5), 1465–1487. https://doi.org/10.1175/JPO-D-20-0214.1

de Bakker, A. T. M., Herbers, T. H. C., Smit, P. B., Tissier, M. F. S., & Ruessink, B. G. (2015). Nonlinear infragravity–wave interactions on a gently sloping laboratory beach. *Journal of Physical Oceanography*, *45*(2), 589–605. https://doi.org/10.1175/JPO-D-14-0186.1

de Bakker, A. T. M., Tissier, M. F. S., & Ruessink, B. G. (2014). Shoreline dissipation of infragravity waves. *Continental Shelf Research*, *72*, 73–82. https://doi.org/10.1016/j.csr.2013.11.013

Donelan, M., Babanin, A., Sanina, E., & Chalikov, D. (2015). A comparison of methods for estimating directional spectra of surface waves. *Journal of Geophysical Research: Oceans*, *120*(7), 5040–5053. https://doi.org/10.1002/2015JC010808

Fiedler, J. W., Smit, P. B., Brodie, K. L., McNinch, J., & Guza, R. T. (2019). The offshore boundary condition in surf zone modeling. *Coastal Engineering*, *143*(April 2018), 12–20. https://doi.org/10.1016/j.coastaleng.2018.10.014

Fujiki, T., Hashimoto, N., & Kawaguchi, K. (2017). Improvement in estimation stability and accuracy of wave directional spectrum by a Bayesian method for swell observation. In *Proceedings of the 27th International offshore and polar engineering conference* (pp. 1355–1362).

Guérin, T., de Bakker, A., & Bertin, X. (2019). On the bound wave phase lag. *Fluids*, *4*(3), 1–17. https://doi.org/10.3390/fluids4030152

Hashimoto, N., & Kobune, K. (1988). Estimation of directional spectrum through a Bayesian approach. *Coastal Engineering Journal*, *31*(2), 183–198. https://doi.org/10.1080/05785634.1988.11924491

Hashimoto, N., Nagai, T., & Asai, T. (1995). Extension of the maximum entropy principle method for directional wave spectrum estimation. In *Coastal engineering 1994* (pp. 232–246). American Society of Civil Engineers. https://doi.org/10.1061/9780784400890.019

Hasselmann, K. (1962). On the non-linear energy transfer in a gravity-wave spectrum part 1. General theory. *Journal of Fluid Mechanics*, *12*(04), 481. https://doi.org/10.1017/S0022112062000373

Hasselmann, K., Munk, W., & MacDonald, G. (1963). Bispectra of ocean waves. In M. Rosenblatt (Ed.), *Time series analysis*. John Wiley.

Henderson, S. M., Guza, R. T., Elgar, S., Herbers, T. H. C., & Bowen, A. J. (2006). Nonlinear generation and loss of infragravity wave energy. *Journal of Geophysical Research*, *111*(12), C12007. https://doi.org/10.1029/2006JC003539

Herbers, T. H. C., Elgar, S., & Guza, R. T. (1994). Infragravity-frequency (0.005–0.05 Hz) Motions on the shelf. Part I: Forced waves. *Journal of Physical Oceanography*, *24*(5), 917–927. https://doi.org/10.1175/1520-0485(1994)024<0917:IFHMOT>2.0.CO;2

Herbers, T. H. C., Elgar, S., & Guza, R. T. (1995). Generation and propagation of infragravity waves. *Journal of Geophysical Research*, *100*(C12), 24863. https://doi.org/10.1029/95JC02680

Herbers, T. H. C., Elgar, S., Guza, R. T., & O'Reilly, W. C. (1995). Infragravity-frequency (0.005–0.05 Hz) Motions on the shelf. Part II: Free waves. *Journal of Physical Oceanography*, *25*(6), 1063–1079. https://doi.org/10.1175/1520-0485(1995)025<1063:IFHMOT>2.0.CO;2

Herbers, T. H. C., Elgar, S., Sarap, N. A., & Guza, R. T. (2002). Nonlinear dispersion of surface gravity waves in shallow water. *Journal of Physical Oceanography*, *32*(4), 1181–1193. https://doi.org/10.1175/1520-0485(2002)032<1181:NDOSGW>2.0.CO;2

Inch, K., Davidson, M., Masselink, G., & Russell, P. (2017). Observations of nearshore infragravity wave dynamics under high energy swell and wind-wave conditions. *Continental Shelf Research*, *138*(December 2016), 19–31. https://doi.org/10.1016/j.csr.2017.02.010

Isobe, M., & Kondo, K. (1985). Method for estimating directional wave spectrum in incident and reflected wave field. In *Coastal Engineering 1984* (Vol. 3, pp. 467–483). American Society of Civil Engineers. https://doi.org/10.1061/9780872624382.033

Janssen, T. T., Battjes, J. A., & van Dongeren, A. R. (2003). Long waves induced by short-wave groups over a sloping bottom. *Journal of Geophysical Research*, *108*(C8), 3252. https://doi.org/10.1029/2002JC001515

Lin, Z., Adcock, T. A. A., & McAllister, M. L. (2022). Estimating ocean wave directional spreading using wave following buoys: A comparison of experimental buoy and gauge data. *Journal of Ocean Engineering and Marine Energy*, *8*(1), 83–97. https://doi.org/10.1007/s40722-021-00218-7

Longuet-Higgins, M. S., & Stewart, R. W. (1962). Radiation stress and mass transport in gravity waves, with application to 'surf beats'. *Journal of Fluid Mechanics*, *13*(04), 481–504. https://doi.org/10.1017/S0022112062000877

Mahmoudof, S. M., & Siadatmousavi, S. M. (2020). Bound infragravity wave observations at the Nowshahr beaches, Southern Caspian Sea. *Applied Ocean Research*, *98*(March), 102122. https://doi.org/10.1016/j.apor.2020.102122

Martins, K., Bonneton, P., & Michallet, H. (2021). Dispersive characteristics of non-linear waves propagating and breaking over a mildly sloping laboratory beach. *Coastal Engineering*, *167*(May), 103917. https://doi.org/10.1016/j.coastaleng.2021.103917

Matsuba, Y., Shimozono, T., & Tajima, Y. (2021a). Extreme wave runup at the Seisho coast during typhoons Faxai and Hagibis in 2019. *Coastal Engineering*, *168*, 103899. https://doi.org/10.1016/j.coastaleng.2021.103899

Matsuba, Y., Shimozono, T., & Tajima, Y. (2021b). Tidal modulation of infragravity wave dynamics on a reflective barred beach. *Estuarine, Coastal and Shelf Science*, *261*(April), 107562. https://doi.org/10.1016/j.ecss.2021.107562

McCall, R. T., Van Thiel de Vries, J. S. M., Plant, N. G., Van Dongeren, A. R., Roelvink, J. A., Thompson, D. M., & Reniers, A. J. H. M. (2010). Two-dimensional time dependent hurricane overwash and erosion modeling at Santa Rosa Island. *Coastal Engineering*, *57*(7), 668–683. https://doi.org/10.1016/j.coastaleng.2010.02.006

Miles, M. D., & Funke, E. R. (1989). A comparison of methods for synthesis of directional seas. *Journal of Offshore Mechanics and Arctic Engineering*, *111*(1), 43–48. https://doi.org/10.1115/1.3257137

Moura, T., & Baldock, T. E. (2017). Remote sensing of the correlation between breakpoint oscillations and infragravity waves in the surf and swash zone. *Journal of Geophysical Research: Oceans*, *122*(4), 3106–3122. https://doi.org/10.1002/2016JC012233

Nielsen, P., & Baldock, T. E. (2010). И-Shaped surf beat understood in terms of transient forced long waves. *Coastal Engineering*, *57*(1), 71–73. https://doi.org/10.1016/j.coastaleng.2009.09.003

Nose, T., Babanin, A., & Ewans, K. (2017). In situ observations of infragravity wave directionality at nearshore coastal sites. *Ocean Science Discussions*, (October), 1–29. https://doi.org/10.5194/os-2017-77

Okihiro, M., Guza, R. T., & Seymour, R. J. (1992). Bound infragravity waves. *Journal of Geophysical Research*, *97*(C7), 11453–11469. https://doi.org/10.1029/92JC00270

Okihiro, M., Guza, R. T., & Seymour, R. J. (1993). Excitation of seiche observed in a small harbor. *Journal of Geophysical Research*, *98*(C10), 18201. https://doi.org/10.1029/93JC01760

Oltman-Shay, J., & Guza, R. T. (1984). A data-adaptive ocean wave directional-spectrum estimator for pitch and roll type measurements. *Journal of Physical Oceanography*, *14*(11), 1800–1810. https://doi.org/10.1175/1520-0485(1984)014<1800:ADAOWD>2.0.CO;2

Plant, W. J., & Donelan, M. A. (2020). Directional surface wave spectra from point measurements of height and slope. *Journal of Atmospheric and Oceanic Technology*, *37*(1), 67–83. https://doi.org/10.1175/JTECH-D-19-0128.1

Rawat, A., Ardhuin, F., Ballu, V., Crawford, W., Corela, C., & Aucan, J. (2014). Infragravity waves across the oceans: Following infra-gravity wave bursts. *Geophysical Research Letters*, *41*(22), 7957–7963. https://doi.org/10.1002/2014GL061604

Rijnsdorp, D. P., Reniers, A. J. H. M., & Zijlema, M. (2021). Free infragravity waves in the North Sea. *Journal of Geophysical Research: Oceans*, *126*(8), 1–14. https://doi.org/10.1029/2021JC017368

Rijnsdorp, D. P., Ruessink, G., & Zijlema, M. (2015). Infragravity-wave dynamics in a barred coastal region, a numerical study. *Journal of Geophysical Research: Oceans*, *120*(6), 4068–4089. https://doi.org/10.1002/2014JC010450

Rijnsdorp, D. P., Smit, P. B., & Zijlema, M. (2014). Non-hydrostatic modelling of infragravity waves under laboratory conditions. *Coastal Engineering*, *85*, 30–42. https://doi.org/10.1016/j.coastaleng.2013.11.011

Roeber, V., & Bricker, J. D. (2015). Destructive tsunami-like wave generated by surf beat over a coral reef during Typhoon Haiyan. *Nature Communications*, *6*(1), 7854. https://doi.org/10.1038/ncomms8854

Roelvink, D., McCall, R., Mehvar, S., Nederhoff, K., & Dastgheib, A. (2018). Improving predictions of swash dynamics in XBeach: The role of groupiness and incident-band runup. *Coastal Engineering*, *134*(February 2017), 103–123. https://doi.org/10.1016/j.coastaleng.2017.07.004

Roelvink, D., Reniers, A., van Dongeren, A., van Thiel de Vries, J., McCall, R., & Lescinski, J. (2009). Modelling storm impacts on beaches, dunes and barrier islands. *Coastal Engineering*, *56*(11–12), 1133–1152. https://doi.org/10.1016/j.coastaleng.2009.08.006

Schäffer, H. A. (1993). Infragravity waves induced by short-wave groups. *Journal of Fluid Mechanics*, *247*(2), 551–588. https://doi.org/10.1017/S0022112093000564

Symonds, G., Huntley, D. A., & Bowen, A. J. (1982). Long wave generation by a time-varying breakpoint. *Journal of Geophysical Research*, *87*(C1), 492–498. https://doi.org/10.1029/JC087iC01p00492

The WAVEWATCH III Development Group. (2016). User manual and system documentation of WAVEWATCH III version 5.16. *Technical Note*.

Thomson, J., Elgar, S., Herbers, T. H. C., Raubenheimer, B., & Guza, R. T. (2007). Refraction and reflection of infragravity waves near submarine canyons. *Journal of Geophysical Research*, *112*(10), 1–9. https://doi.org/10.1029/2007JC004227

Ursell, F. (1952). Edge waves on a sloping beach. *Proceedings of the Royal Society of London. Series A. Mathematical and Physical Sciences*, *214*(1116), 79–97. https://doi.org/10.1098/rspa.1952.0152

van Dongeren, A., Battjes, J., Janssen, T., van Noorloos, J., Steenhauer, K., Steenbergen, G., & Reniers, A. (2007). Shoaling and shoreline dissipation of low-frequency waves. *Journal of Geophysical Research*, *112*(C2), C02011. https://doi.org/10.1029/2006JC003701

Winter, G., Lowe, R. J., Symonds, G., Hansen, J. E., & van Dongeren, A. R. (2017). Standing infragravity waves over an alongshore irregular rocky bathymetry. *Journal of Geophysical Research: Oceans*, *122*(6), 4868–4885. https://doi.org/10.1002/2016JC012242

Zijlema, M., Stelling, G., & Smit, P. (2011). SWASH: An operational public domain code for simulating wave fields and rapidly varied flows in coastal waters. *Coastal Engineering*, *58*(10), 992–1012. https://doi.org/10.1016/j.coastaleng.2011.05.015